

# Narrow absorption lines from intervening material in supernovae

## IV. Type Ia supernovae: NaID line strength relating to external material and intrinsic properties

Santiago González-Gaitán<sup>1</sup> , Claudia P. Gutiérrez<sup>2,3</sup> , João Duarte<sup>4</sup>, Rita Santos<sup>4</sup>, Gonçalo Martins<sup>4</sup>, Joseph P. Anderson<sup>5</sup> , and Lluís Galbany<sup>3,2</sup> 

<sup>1</sup> Instituto de Astrofísica e Ciências do Espaço, Faculdade de Ciências, Universidade de Lisboa, Ed. C8, Campo Grande, 1749-016 Lisbon, Portugal  
e-mail: gongsale@gmail.com

<sup>2</sup> Institut d'Estudis Espacials de Catalunya (IEEC), Edifici RDIT, Campus UPC, 08860 Castelldefels (Barcelona), Spain  
e-mail: cgutierrez@ice.csic.es

<sup>3</sup> Institute of Space Sciences (ICE, CSIC), Campus UAB, Carrer de Can Magrans, s/n, E-08193 Barcelona, Spain

<sup>4</sup> CENTRA, Instituto Superior Técnico, Universidade de Lisboa, Av. Rovisco Pais 1, 1049-001 Lisboa, Portugal

<sup>5</sup> European Southern Observatory, Alonso de Córdova 3107, Casilla 19, Santiago, Chile

### ABSTRACT

Type Ia supernovae (SNe Ia) are thermonuclear runaways in certain white dwarfs in binary systems. They have been extensively studied, yet their progenitor and explosion mechanisms remain poorly understood. We study a large sample of SNe Ia comparing the narrow interstellar absorption features in their spectra with various photometric and spectroscopic supernova properties, as well as with environmental characteristics. We find that the sodium absorption is significantly stronger in younger, more star-forming and more centrally located SNe Ia, as expected. However, we also show that there is a strong dependence on intrinsic properties that is independent of the environment. In fact, we find strong evidence for two environmental SN Ia populations, an old and a young one, with the young population showing significantly different distributions of sodium strength when divided according to the Si II ejecta velocity, nebular velocity, extinction,  $E(B-V)$ , and reddening curve,  $R_V$ . Performing a clustering of the SNe Ia, we recover an old population of SNe with low extinction and normal ejecta velocity, while we confirm that the young population can be subdivided into a group of highly-extincted, high-velocity SNe Ia with much stronger blueshifted sodium absorption, and another of low-extincted, normal-velocity objects with little sodium absorption. We interpret this relation of intervening material with intrinsic properties as evidence for the young SN Ia population, occurring in young and star-forming environments, to have asymmetric radiation that interacts with nearby material, and whose observables depend thus on the viewing angle. Finally, we show that the cosmological mass-step is consistent with these populations.

**Key words.** supernovae: general, ISM: lines and bands, dust

### 1. Introduction

Type Ia supernovae (SNe Ia) are fascinating bright explosions that mark the end stages of some binary stellar systems, enrich the Universe with heavy elements (e.g., Matteucci & Recchi 2001; Cavichia et al. 2024), and are routinely used to measure distances in cosmology (e.g., Riess et al. 1998; Perlmutter et al. 1999; DES Collaboration et al. 2024). Although there is consensus that they originate from the thermonuclear runaway of a carbon-oxygen white dwarf (WD; e.g., Nugent et al. 2011; Bloom et al. 2012), many questions remain on the nature of the companion star and the explosion process (see Ruiter & Seitzenzahl 2025 for a review).

Progenitor systems have traditionally been subdivided into single-degenerate (SD) systems, in which the companion is a non-degenerate main-sequence, helium or red giant star (Whelan & Iben 1973), and double-degenerate (DD) scenarios, in which the companion is another degenerate WD (Iben & Tutukov 1984); but alternative progenitors have been proposed (e.g., Wang et al. 2017; Soker & Bear 2023). The main explosion scenarios of SNe Ia are: i) the Chandrasekhar-mass ( $M_{\text{Ch}}$ ) model in which the WD nears the Chandrasekhar limit of  $1.4M_{\odot}$  leading to a defla-

gration at the centre that transitions into a detonation (delayed-detonation, Nomoto et al. 1984; Khokhlov 1991), and ii) the sub-Chandrasekhar (sub- $M_{\text{Ch}}$ ) model in which the WD accretes helium from a companion that detonates in the outer shell leading to a sub- $M_{\text{Ch}}$  detonation in the core (double-detonation or DDet, Taam 1980; Nomoto 1980). More recent studies have shown that a smaller helium shell at ignition agrees better with observations (Bildsten et al. 2007; Shen & Bildsten 2009), motivating numerous further studies (e.g., Kromer et al. 2010; Townsley et al. 2012; Shen et al. 2021). Theoretical and observational considerations have shown that multiple mechanisms may combine to produce the overall "normal" SN Ia population (e.g., Ruiter et al. 2009; Scalzo et al. 2014; Dhawan et al. 2017; Cikota et al. 2026), without even considering outlying peculiar objects (e.g., Filippenko et al. 1992; Phillips et al. 1992; Li et al. 2003).

The main mechanism powering the light-curve of SNe Ia is the radioactive decay of nickel, and successful models need to be able to explain, among other observations, the relation between maximum brightness and light-curve width (Phillips 1993), which is also one of the corrections for distance calibration. In addition to the presence of both iron-group elements and

intermediate-mass elements in the spectra, models must be able to reproduce a range of ejecta velocities and absorption strengths (Branch et al. 2006; Wang et al. 2009).

Another part of the puzzle of SN Ia progenitors is the possible presence of detached material near the explosion. Some SNe Ia show clear evidence for this material through narrow hydrogen emission lines in their spectra (Hamuy et al. 2003; Dilday et al. 2012; Sharma et al. 2023), infrared excess and radio emission (Mo et al. 2025; Kool et al. 2023), light-echoes (e.g., Wang et al. 2008; Drozdov 2016), varying narrow absorption features (e.g., Blondin et al. 2009; Sternberg et al. 2014; Ferretti et al. 2016) that are blueshifted (e.g., Sternberg et al. 2011; Maguire et al. 2013; Phillips et al. 2013), among others. If such matter is circumstellar material (CSM) produced prior to the explosion, either from accretion or merger events, this provides very relevant information on the progenitor system (e.g., Piro & Morozova 2016; Moriya et al. 2023; Inoue et al. 2025). If it comes from close-by interstellar clouds, then this also has important implications for the physics of the interstellar medium (ISM).

Associated with the question of nearby material, dust extinction in the line of sight of SNe Ia has been a continuously active subject of debate. As the amount of dust changes from object to object, the reddening alters the observed colours and the associated extinction dims the light. This explains the linear trend observed in the brightness-colour relation of SNe Ia, although it is expected both theoretically and observationally that intrinsic colours vary (e.g., Burns et al. 2014; Hoeflich et al. 2017). To complicate things further, a few SNe Ia present very peculiar reddening curves (e.g. Foley et al. 2014; Gutiérrez et al. 2016) and possible variations with environments (Ramaiya et al. 2025; Duarte et al. 2025). Moreover, there is evidence that a non-negligible fraction of SNe Ia suffer variable extinction (Förster et al. 2013; Bulla et al. 2018). These observations could pose problems to the simple linear brightness-colour relation of SNe Ia, i.e. the second correction of the distance calibration (Tripp 1998). In fact, a third brightness correction related to the environment of the SNe Ia ("mass-step", see e.g. Sullivan et al. 2010; Kelly et al. 2010) seems to be related to dust and/or intrinsic colours (e.g., Brout & Scolnic 2021; González-Gaitán et al. 2021).

In this paper, we analyse a large sample of SNe Ia focusing on the narrow absorption spectral lines of intervening material in the line of sight and compare their equivalent width and velocity to environmental and supernova properties, to shed more light on the ongoing question of the progenitors, the nearby material and the colours and extinction of SNe Ia. This is the fourth paper of a series: in the first paper we present the full dataset comprising all SN types and the automated techniques to measure the lines, as well as a study of their evolution with time (González-Gaitán et al. 2024, hereafter Paper I), in the second paper we compare the narrow lines to environmental properties (González-Gaitán et al. 2025, hereafter Paper II), and in the third we analyse differences among SN types (Gutiérrez et al. 2026, hereafter Paper III). This paper, dedicated to SNe Ia, is organised as follows: Sect. 2 describes the data, measurements and methodology, Sect. 3 the analysis and results, Sect. 4 discusses our results and Sect. 5 presents our conclusions.

## 2. SN sample and their properties

Throughout this series of papers, we used a historical sample of nearby SNe that has both spectra and photometry in various bands. The SN Ia sample after cuts (see Sect. 2.1) is composed of 981 objects (with 3230 spectra). The sample contains only

**Table 1.** SN and environmental properties used in this study.

Property	Nr SNe Ia	MED	MAD	Source
<b>Narrow line of Na I D (§ 2.1)</b>				
EW(Å)	514	0.278	0.493	Paper I
VEL(km s <sup>-1</sup> )	327	4.0	83.9	Paper I
<b>Environmental properties (§ 2.2)</b>				
$\Delta\alpha$	834	0.203	0.107	Paper II
$\log \text{SFR}^L(\text{M}_\odot \text{yr}^{-1})$	359	-3.15	1.42	Paper II
$\log \text{sSFR}^L(\text{yr}^{-1})$	359	-11.81	0.27	Paper II
$t_{\text{age}}^L(\text{Gyr})$	359	1.51	1.28	Paper II
$A_V^L$	359	2.58	0.72	Paper II
$\log M_*^L(\text{M}_\odot)$	359	7.96	0.72	Paper II
$\log M_*^G(\text{M}_\odot)$	873	10.84	0.70	Paper II
<b>Photometric properties (§ 2.3)</b>				
$s$	427	0.956	0.097	This work*
$C$	425	0.075	0.110	This work*
$SBV$	404	0.929	0.107	This work <sup>†</sup>
$EBV$	404	0.208	0.100	This work <sup>†</sup>
$R_V$	404	3.285	1.300	This work <sup>†</sup>
$dBV_{60}(\text{mag d}^{-1})$	177	-0.011	0.003	This work*
$BV_{60}$	177	0.839	0.152	This work*
<b>Spectral properties (§ 2.4)</b>				
$v_{\text{max}}(\text{km s}^{-1})$	274	-10937	739	This work
$v_{\text{grad}}(\text{km s}^{-1} \text{d}^{-1})$	144	73.8	35.7	This work
$v_{\text{neb}}(\text{km s}^{-1})$	44	505	1165	This work
<b>Hubble residuals (§ 2.5)</b>				
HR	285	-0.010	0.097	This work*
$HR_L$	182	-0.002	0.104	This work*
$HR_G$	259	0.000	0.101	This work*

**Notes.** Property, number of SNe with finite EW and property, median (MED), median absolute deviation (MAD) and source.

\* Using SiFTO

<sup>†</sup> Using SNoPy

★ Following Förster et al. (2013)

♣ Using Brout et al. (2022a)

a few peculiar objects, such as Iax (8), 91bg-like (2), 91T-like (1) and super-Chandra (3). We will compare the narrow lines measurements from intervening material such as Na I D with SN and host properties. A list of those properties and their median is provided in Tab. 1, whereas in App. C we provide the full set of parameters for all SNe Ia in this study.

### 2.1. Narrow line measurements

We developed a robust automatic tool to measure the equivalent width (EW in Å) and velocity shift (VEL in km/s) of the narrow lines, as explained in Paper I. Since we found no evolution with time, when several spectra at different epochs exist for a given SN, we stack the flux-to-continuum ratios of each spectrum and do a bootstrap analysis. It is important to note that for low-resolution spectra, the P-Cygni profile of the fast-moving ejecta may interact with the profile of the slow-moving narrow line, thus altering the EW measurement and leading to erroneous conclusions. By applying a continuum slope cut around the line, we make sure to use spectra for which this interference is minimal. Together with a signal-to-noise cut around the line, the initial sample of 1079 SNe Ia (with 3534 spectra) is reduced to 981 objects (with 3230 spectra). Our automated technique integrates a fixed region that, in the case of noise or emission lines, can result in negative EW values. For the velocity measurement, we only consider

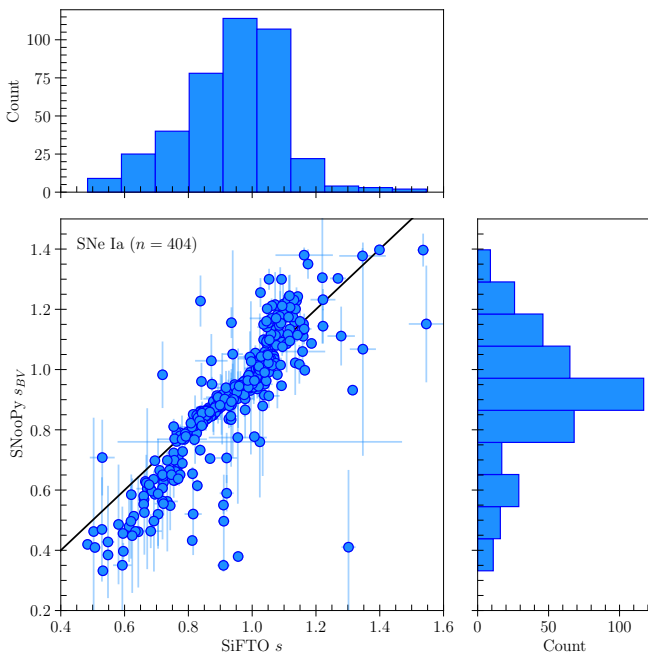


**Fig. 1.** SNooPy  $s_{BV}$  vs SiFTO  $s$  light-curve width parameters for SNe Ia in our sample with their corresponding histograms in the panels.

cases with  $|\text{EW}| > 0.3\text{\AA}$  to ensure there is enough absorption to calculate the wavelength of the minimum.

## 2.2. Environmental parameters

In Paper II we introduced the environmental parameters calculated for our SN sample. By taking available multi-band images of the SN host galaxies from UV to IR, we do both: i) global photometry using Kron apertures and ii) local photometry taking apertures of 0.5 kpc in radius. The photometry is then fitted to composite stellar populations with a dust attenuation law to extract global and local parameters such as the stellar mass  $M_*^L(M_\odot)$ , the stellar age  $t_{\text{age}}^L(\text{Gyr})$ , the star formation rate  $\text{SFR}^L(M_\odot \text{yr}^{-1})$  and specific star formation rate  $\text{sSFR}^L(\text{yr}^{-1})$ , the dust attenuation  $A_V^L$ , among others. We focus here on these five local parameters, which are the ones showing the strongest relations to the narrow lines (Paper II), as well as on the offset of the SN from the host centre normalised by the semi-major axis,  $\Delta\alpha$ . We also include the global mass  $M_*^G(M_\odot)$  because of its relevance for cosmology (see Sect. 2.5).

## 2.3. Photometric properties

In this paper, we will compare the EW and VEL of the narrow lines with SN properties. The main photometric properties are the light-curve width, also known as the stretch parameter  $s$ , and the observed  $B-V$  colour  $C$  at maximum. These are obtained through multi-band light-curve fits with the SiFTO software (Conley et al. 2008). With the SNooPy fitter (Burns et al. 2014), we also obtain the colour-stretch parameter,  $s_{BV}$ , which is related to the width of the colour-curve, along with the dust colour excess,  $EBV \equiv E(B-V)$  and the dust extinction law parametrised by the total-to-selective extinction ratio,  $R_V = A_V/E(B-V)$ . SNooPy, as opposed to SiFTO, assumes an intrinsic colour that depends on  $s_{BV}$  from which the dust extinction and its wavelength dependence can be extracted assuming a reddening law

parametrisation (Cardelli et al. 1989; O'Donnell 1994, CCM). Near-infrared (NIR) photometry, when available, greatly helps anchor the reddening curve. A distribution of these parameters for our sample is shown in Figures 1 and 2. Individual example fits are shown in App. A.1. As can be seen, the  $R_V$  spans a wide range of values beyond the Milky Way (MW) star observations with which the CCM law was obtained ( $2.6 < R_V < 5.6$ , Fitzpatrick 1999). Beyond  $R_V \sim 5$ , the reddening curve in the optical and NIR changes minimally, so that very high  $R_V$  values are basically consistent with lower values, and this is well reflected in the larger error bars. Importantly, as well, SNe with little extinction are more difficult to fit and have very uncertain  $R_V$  estimates, stressing the importance of the prior (see App. A.1).

We also investigate the photometric properties after the main part of the light-curve, between 35 and 85 days past maximum. This period, also known as the Lira law (Phillips et al. 1999), is known for having a homogeneous linear decline in colour and is possibly a better telltale of the true line-of-sight extinction. Furthermore, Förster et al. (2013) found a possible trend between the rate of colour decline and the EW of sodium that is worth exploring further. We thus use here late-time MW and  $K$ -corrected  $B$  and  $V$  photometry to calculate two parameters: the Lira-law  $B-V$  slope  $dBV_{60} \equiv d(B-V)/dt|_{60d}$  in mag/day, and the corresponding late-time colour  $BV_{60} \equiv (B-V)_{60d}$ .

We thus have seven photometric parameters:  $s$ ,  $C$ ,  $s_{BV}$ ,  $EBV$ ,  $R_V$ ,  $dBV_{60}$  and  $BV_{60}$ . Three of those should in principle be only related to the explosion, i.e. they are *intrinsic* properties to the SN and reflect their inner evolution:  $s$  and  $s_{BV}$  represent the main evolution and are closely related to each other (see Fig. 1), as well as  $dBV_{60}$  which describes the late evolution. On the other hand,  $EBV$  and  $R_V$  are purely *extrinsic* parameters (assuming the intrinsic colours are well modelled) coming from dust extinction. Finally, the observed colours at maximum,  $C$ , and at late times,  $BV_{60}$ , are a combination of intrinsic and extrinsic factors.

## 2.4. Spectral properties

A key spectroscopic property that describes the variability of SNe Ia is the Si II (6355\AA) expansion velocity near maximum (Benetti et al. 2005). Moreover, as we peer into deeper layers of slower-moving ejecta with time, the velocity gradient is also an important spectroscopic characteristic of the SN evolution (Wang et al. 2009). We use our own semi-automatic code to measure the velocities of the Si II absorption profile. To define the continuum of the line, we use the same blue-ward and red-ward wavelength ranges of Folatelli et al. (2013). We then calculate the minimum of the smoothed line profile inside these bounds to obtain the wavelength shift and the expansion velocity. This is done for all available spectra of a given SN. We require at least one spectrum within  $\pm 3$  days of  $B$ -band maximum light to calculate the  $v_{\text{max}}(\text{km s}^{-1})$  parameter from a linear interpolation. For the velocity decline rate, we estimate an expansion velocity similarly at 20 days after maximum from spectra  $\pm 5$  around that date, and use:  $v_{\text{grad}} = (v_{\text{max}} - v_{20})/20$  (Blondin et al. 2012). Fig. 3 shows these parameters for our sample. Some individual examples and more details are given in App. A.2.

We also investigate a very different spectroscopic regime when the SN has reached the nebular phase. At these times ( $\gtrsim 100$  d), we are observing the innermost part of the ejecta and the shifts of forbidden lines synthesized near the centre of the explosion such as [Ni II]  $\lambda 7378\text{\AA}$  and [Fe II]  $\lambda 7378\text{\AA}$   $7155\text{\AA}$  are useful to infer the explosion asymmetry (e.g. Maeda et al. 2010). We use the same spectral literature sample as in Paper I to look for

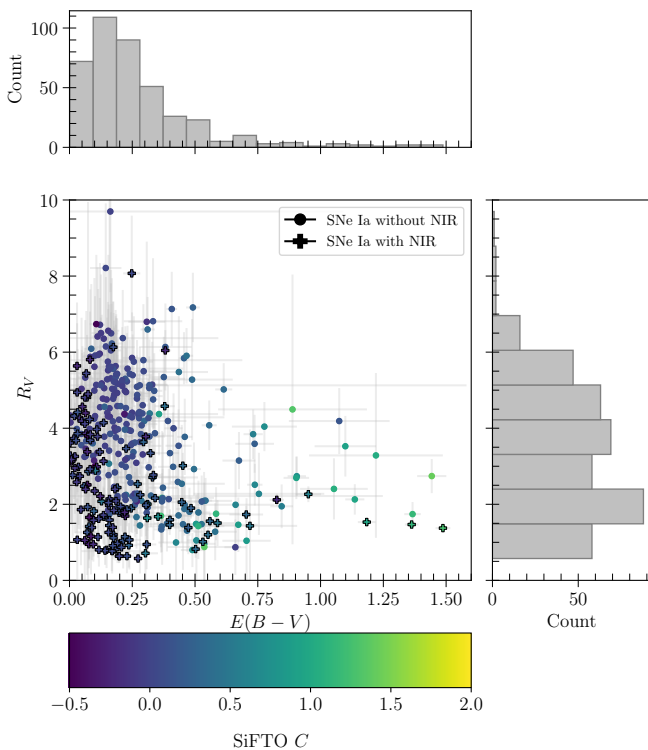


**Fig. 2.** SNooPy  $R_V$  vs  $EBV$  parameters for SNe Ia in our sample with their corresponding histograms in the panels. The point colours indicate the SiFTO colour  $C$ . Crosses indicate SNe with NIR used in the fits.

nebular spectra, finding 194 spectra for 64 SNe Ia. We measure their nebular velocity,  $v_{neb}$ , following the procedure described by Maeda et al. (2011). When both nebular emission lines [Ni II]

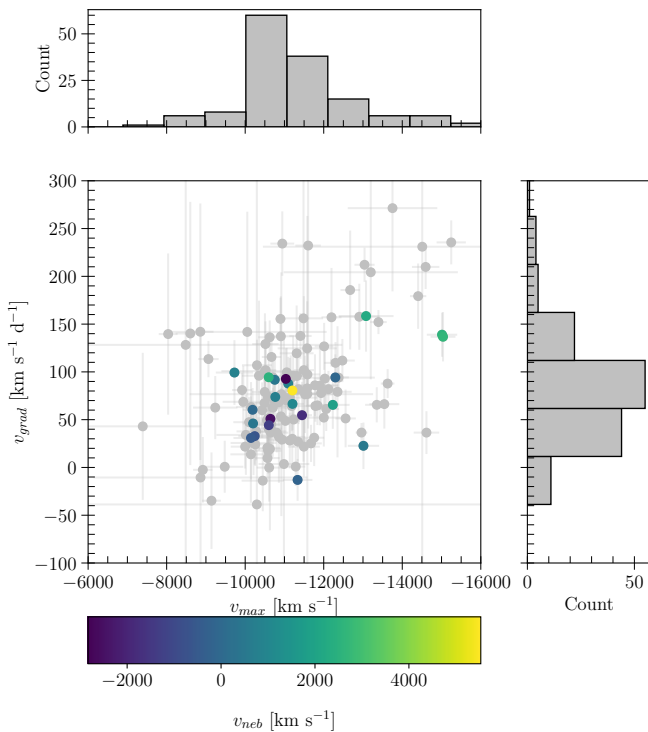


**Fig. 3.** Velocity gradient vs velocity at maximum for Si II (6355 Å) and their corresponding histograms. The point colours indicate the nebular velocity when available.

$\lambda 7378\text{\AA}$  and [Fe II]  $\lambda 7378\text{\AA}$   $7155\text{\AA}$ , are detected, we determine the line shifts by fitting each feature with a Gaussian profile. The  $v_{neb}$  is then defined as the mean velocity derived from the two lines. In cases where only one of the two lines is detected,  $v_{neb}$  is measured using the available line alone. Many of the analysed SNe already had measurements that agree with our estimates (Maeda et al. 2011; Silverman et al. 2012; Blondin et al. 2012).

### 2.5. Hubble residuals

SNe Ia have been extensively used as distance indicators for cosmology (e.g. Riess et al. 2022; Popovic et al. 2025). As imperfect standard candles, their luminosity needs to be corrected for at least two parameters, the light-curve width and the colour. A third correction relating to the environment of the host galaxy, often represented by the host stellar mass (e.g. Sullivan et al. 2010; Lampeitl et al. 2010), accounts for additional variations not captured in the first two corrections. This third correction, also known as the "mass-step", has gathered significant attention in recent years, questioning its origin: extrinsic due to dust extinction, intrinsic due to differing SN properties, or a combination of both (e.g. Brout & Scolnic 2021; González-Gaitán et al. 2021; Duarte et al. 2023; Wiseman et al. 2023).

In this work, we also study the dependence of the cosmology on the narrow lines of intervening material. For this, we calculate the Hubble residuals using the SN parameters given in Brout et al. (2022a), notably the light-curve width  $x_1$  and the colour at maximum  $c$  obtained with the SALT fitter (Guy et al. 2007, 2010; Brout et al. 2022b). We assume a fixed  $\Lambda$ CDM cosmology with  $H_0 = 73 \text{ km s}^{-1} \text{ Mpc}^{-1}$ ,  $\Omega_M = 0.30$  and  $\Omega_\Lambda = 0.70$ , so that:

$$\text{HR} = \mu_{\text{SN}}(M_B, \alpha, \beta, \Delta_{\text{host}}) - \mu_{\text{cosmo}}(z, H_0, \Omega_M, \Omega_\Lambda),$$

with:

$$\mu_{\text{cosmo}} = 5 \log(d_L/10\text{pc}),$$

where  $d_L$  is the cosmology-dependent luminosity distance, and

$$\mu_{\text{SN}} = m_B - M_B + \alpha x_1 - \beta c + \delta_{\text{host}},$$

with the mass-step given by:

$$\delta_{\text{host}} = \begin{cases} \Delta_{\text{host}}, & \text{if } M < M_{\text{step}} \\ -\Delta_{\text{host}}, & \text{if } M > M_{\text{step}} \end{cases}$$

with  $M_{\text{step}}$  taken as the median of the sample.

The parameters  $M_B$ ,  $\alpha$ ,  $\beta$  and  $\Delta_{\text{host}}$  are free parameters of the cosmological fit. We perform fits and obtain Hubble residuals (HR) for three cases: one without a mass-step, another with a local mass-step obtained here from the stellar mass within the  $r = 0.5 \text{ kpc}$  aperture, and a third one with a global mass-step from the stellar mass of the full Kron aperture (see Sect. 2.2). The Hubble residuals of these three fits are called: HR,  $\text{HR}_L$  and  $\text{HR}_G$ , and they do not include bias corrections. However, we emphasise that in this study, our objective is not to obtain accurate cosmological fits and standardisation parameters, but to explore the relative differences of HR with narrow lines of SNe. Tab. 2 summarises the fitted parameters. More details can be found in App. A.3.

## 3. Analysis and Results

In this section, we analyse the narrow line properties, particularly the EW of Na I D, compared to the different intrinsic and extrinsic properties presented in the previous section. To do this, we employ mainly statistical means to compare the property

**Table 2.** Standardisation parameters from cosmological fits.

Par \ Fit	No $\delta_{\text{host}}$ (HR)	Local $\delta_{\text{host}}$ ( $\text{HR}_L$ )	Global $\delta_{\text{host}}$ ( $\text{HR}_G$ )
$N_{\text{SN}}$	359	195	277
$M_B$	-19.215(10)	-19.184(24)	-19.186(17)
$\alpha$	0.155(09)	0.166(14)	0.166(11)
$\beta$	2.690(112)	2.834(185)	2.695(176)
$\Delta_{\text{host}}$	-	-0.067(31)	-0.073(25)
$\sigma_{\text{int}}$	0.105(12)	0.122(21)	0.103(28)
RMS	0.234	0.245	0.211

distributions. The Kolmogorov-Smirnov (KS) test (Kolmogorov 1933; Smirnov 1939) permits testing the hypothesis that two different distributions of a single quantity arise from the same parent population. The Fasano-Franceschini (FF) test (Fasano & Franceschini 1987), on the other hand, extends the KS test to the comparison of two samples with multiple properties. In both cases, a p-value lower than 0.05 rejects the hypothesis that both samples come from the same parent population. In Paper I and Paper II, we also consider a bootstrap analysis that ensures that both compared distributions are consistent in redshift, while allowing the dividing value between both samples to be swept between 40-60% of the full distribution to obtain a final median p-value with a corresponding probability ( $P_{MC}$ ) of being lower than 0.05. In Sect. 3.1, we study the narrow line EW distributions when divided according to single properties, in Sect. 3.2 we repeat the study, ensuring that the environments of the compared SN properties are more consistent, while in Sect. 3.3 we obtain SN groups with a clustering analysis and investigate their narrow line characteristics.

### 3.1. $\text{Na I D}$ EW distributions

We start by highlighting that the strong trends found in Paper II of  $\text{Na I D}$  EW with local host properties are maintained with SNe Ia: there is a stronger abundance of sodium in SNe Ia located in central regions and local environments that are more star-forming, younger, more massive and that have a higher dust attenuation. These findings, summarised in Tab. 3, are obtained from individual KS tests that divide the SN sample into two groups, according to the median of the property considered (see Tab. 1 for the median values) or values swept around the median for the bootstrap probability. All the p-values are well below 0.05, and their probabilities are above 80% (except for  $A_V^L$ ). This is also consistent with the local  $H\alpha$  from the host relating to  $\text{Na I D}$  EW for SNe Ia, as found in Anderson et al. (2015). For the global mass, we do not find that the two EW distributions are different from each other, confirming that  $\text{Na I D}$  is a tracer of local gas abundance (see Paper II) and that local and global properties do not follow a one-to-one relation.

Regarding the SN properties, we see that the light-curve width, parametrised both by  $s$  and  $s_{BV}$ , shows a strong relation with the EW of  $\text{Na I D}$  ( $P_{MC} \sim 90\%$ ). This is expected as high-stretch SNe Ia are known to occur in younger and more star-forming regions (e.g., Hamuy et al. 1995, 1996), so there is a stronger abundance of gas and dust around them. The observed colour  $C$  is highly correlated with the EW ( $p \sim 1e^{-5}$ ,  $P_{MC} = 100\%$ ; see also Anderson et al. 2015), confirming that the sodium abundance is a good tracer of dust extinction. This is even more evident when we use the colour excess,  $EBV$  ( $p \sim 1e^{-11}$ ,  $P_{MC} = 100\%$ ), which is in principle exclusively due to extinc-

**Table 3.** KS tests of two EW distributions divided according to a single property.

Property	$\langle \text{EW}_{\text{hi}} \rangle$	$\langle \text{EW}_{\text{lo}} \rangle$	KS*	$P_{MC}^{\dagger}$
<b>Environmental properties</b>				
$\Delta\alpha$	0.08±0.29	0.71±0.66	3.80e-15	100(100)
$\log \text{SFR}^L$	0.84±0.69	0.09±0.26	7.56e-10	100(100)
$\log \text{sSFR}^L$	0.73±0.69	0.12±0.28	8.33e-7	100(98)
$t_{\text{age}}^L$	0.13±0.31	0.61±0.63	1.29e-4	92(67)
$A_V^L$	0.59±0.63	0.19±0.38	4.67e-2	41(9)
$\log M_*^L$	0.73±0.73	0.13±0.28	2.10e-6	100(97)
$\log M_*^G$	0.28±0.51	0.39±0.54	2.96e-1	10(2)
<b>Photometric properties</b>				
$s$	0.37±0.45	0.18±0.46	3.20e-3	88(50)
$C$	0.61±0.67	0.08±0.33	1.19e-5	100(97)
$s_{BV}$	0.41±0.45	0.13±0.48	1.56e-4	90(63)
$EBV$	0.80±0.66	0.01±0.26	1.74e-11	100(98)
$R_V$	0.21±0.43	0.37±0.52	2.69e-1	19(4)
$dBV_{60}$	0.17±0.37	0.15 ± 0.36	6.21e-1	6(0)
$BV_{60}$	0.54±0.51	-0.06 ± 0.18	8.05e-8	100(98)
<b>Spectral properties</b>				
$v_{\text{max}}$	0.37±0.54	0.30±0.45	3.22e-1	9(1)
$v_{\text{grad}}$	0.24±0.49	0.26±0.32	1.37e-1	15(2)
$v_{\text{neb}}$	0.63±0.68	-0.05 ± 0.16	1.38e-2	34(6)
<b>Hubble residuals</b>				
$\text{HR}$	0.15±0.39	0.13±0.38	9.09e-1	5(0)
$\text{HR}_L$	0.30±0.35	0.12±0.28	3.25e-1	9(1)
$\text{HR}_G$	0.24±0.40	0.12±0.37	8.71e-1	6(0)

**Notes.** Property, median and MAD EW(Å) of  $\text{Na I D}$  for the upper/lower half of the property sample, raw KS test and bootstrap probability (%) for the p-value<0.05 (<0.01 in parentheses).

\* Raw KS test between EW distributions divided by their median

† Bootstrap probability (%) of p-value<0.05 (<0.01) between  $z$ -matched EW distributions divided by sweeping values within 40-60%

tion without intrinsic colour variations. Similarly, the observed colour in the Lira law regime, i.e. 60 days after maximum, is indeed a better tracer of the extinction than at maximum light ( $p \sim 1e^{-8}$ ,  $P_{MC} = 100\%$ ), as the intrinsic variations among SNe Ia have decreased by that time.

Interestingly, splitting the sample according to the nebular velocity shows strong differences in EW (see Fig. 4) with a p-value of 0.014. The low  $v_{\text{neb}}$  sample has a median EW of -0.05Å compared to 0.63Å for the high  $v_{\text{neb}}$  sample. The bootstrap probability is rather small (34%), but this is due to the small sample size of 44 SNe. Such a trend was already found in Förster et al. (2012) and indicates a relation between intrinsic SN properties, i.e. the asymmetry of the explosion, and its surrounding material.

Other parameters do not show significant p-values and high bootstrap probabilities, but have interesting differences in their median EW values. SNe Ia with lower  $R_V$  have higher EW (0.40 vs 0.24Å), a result that agrees with previous findings of higher extinction for steeper reddening laws (e.g., Mandel et al. 2011; Burns et al. 2014). The Hubble residuals corrected for mass-step (both local and global) have median EW values that are larger for higher HR compared to lower HR (0.30 vs 0.12Å). This is an interesting result that we explore further in Sect. 4.5.

### 3.2. $\text{Na I D}$ EW distributions in similar environments

In the previous section, we found important differences in  $\text{Na I D}$  EW absorption according to various SN properties. However, this may be entirely driven by the dependence of SN properties (e.g.,

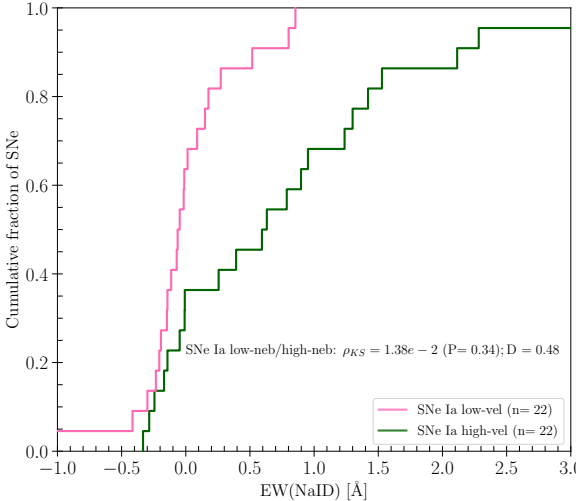


**Fig. 4.** Cumulative distributions of Na I D EW divided according to the median of the nebular velocity  $v_{neb}$ .

**Table 4.** Median (and median absolute deviation) for environmental properties of two subsamples: young (YG) and old (OLD).

Sub-sample	Nr	$\langle sSFR^L \rangle$	$\langle SFR^L \rangle$	$\langle t_{age}^L \rangle$	$\langle A_V^L \rangle$	$\langle M_*^L \rangle$
OLD	222	-12.1(0.1)	-4.3(1.2)	2.8(2.0)	2.6(0.9)	7.7(0.9)
YG	137	-10.5(0.6)	-1.5(0.7)	0.3(0.3)	2.6(0.5)	8.3(0.5)

**Notes.** The values are logarithmic for sSFR, SFR and  $M_*$ .

stretch) on the host. In order to exclude these effects, we attempt to divide the sample according to the environments.

We use the multi-dimensional version of the KS test, the FF test, which combines multiple properties of two samples to find a p-value giving the probability that these two samples do not arise from the same parent population. We explore a division that separates the best two samples according *only* to their local environmental properties of SFR, sSFR, age, dust attenuation and stellar mass. This experiment (see App. B.1 for details) results in a best division of local  $\log(sSFR) = -11.3$  that splits the sample into two populations of SNe Ia with strongly differing environments. We call these the "old" and "young" subsamples (see Tab. 4). Two environmental populations of SNe Ia have been suggested early in the literature with a prompt (younger stellar populations) and a delayed (older stellar populations) channel (Mannucci et al. 2005; Sullivan et al. 2006). More recently, less-biased samples of SNe Ia find evidence for bimodal distributions, particularly in the light-curve width parameter (Nicolas et al. 2021; Ginolini et al. 2025), which strongly correlates with environment. In our case, the division is rather arbitrary but provides a means to study the EW distributions in more detail.

After separating the sample into two subpopulations with significantly different environments, we repeat the individual KS tests of the EW distributions divided according to SN properties for each of these two environmental subsamples. The results are summarised in Tab. 5 for the old (left) and young (right) components, respectively. Despite the division into two environmental populations, there might be non-discrete variations with environment within each subsample considered. We therefore add a column that provides the FF test of the two property populations arising from the same distribution based on all local properties.

For the old population, we find that the EW distributions divided according to the light-curve width ( $s$  and  $s_{BV}$ ) show signifi-

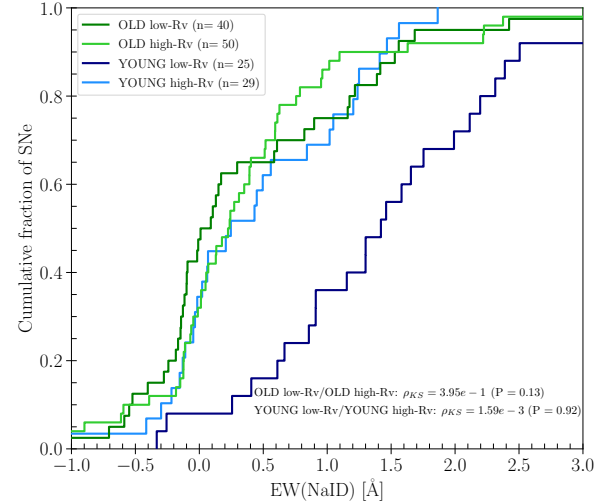


**Fig. 5.** Cumulative distributions of Na I D EW divided according to the median of the  $R_V$  (top) and the  $v_{max}$  (bottom) for the old and young subsamples.

cant differences ( $p < 0.04$ ) which probably are still entirely driven by environmental differences, as the FF p-values are also significant (at least for  $s$  with  $p < 0.05$ ). On the other hand, the observed colour at maximum ( $C$ ) and during the Lira regime ( $BV_{60}$ ), as well as the colour excess  $EBV$ , have significantly different EW distributions with simultaneously consistent environments (FF  $p > 0.4$ ), indicating that there are important dust variations in the SN environments at scales smaller than those probed by our local estimates of  $r = 0.5$  kpc. Moreover, the nebular velocity stands out again, as SNe with high redshifted velocities show stronger sodium absorption. Finally, the Hubble residuals corrected for mass-step show relevant differences in EW, particularly for the local mass-step ( $p = 0.013$ ), with higher HR values (fainter after other corrections) having larger EWs.

For the young component, the division according to light-curve width results in consistent EW distributions. However, the  $EBV$  and  $R_V$  parameters have significant p-values revealing that SNe Ia, which are more extinguished and with lower  $R_V$ , possess a much larger abundance of sodium ( $\gtrsim 1.2\text{\AA}$ ) than their counterparts ( $\lesssim 0.25\text{\AA}$ ). These large differences in EW are also seen for populations divided according to the ejecta velocity (SNe with

**Table 5.** KS tests of two EW distributions divided according to a single property for two environmental subsamples: old (left), young (right).

Subsample	OLD					YOUNG				
Property	$\langle \text{EW}_{\text{hi}} \rangle$	$\langle \text{EW}_{\text{lo}} \rangle$	KS*	$\text{PMC}^{\dagger}$	$\text{FF}_{\text{env}}^{\triangle}$	$\langle \text{EW}_{\text{hi}} \rangle$	$\langle \text{EW}_{\text{lo}} \rangle$	KS*	$\text{PMC}^{\dagger}$	$\text{FF}_{\text{env}}^{\triangle}$
Environmental properties										
$\Delta\alpha$	0.01 $\pm$ 0.20	0.59 $\pm$ 0.58	6.97e-4	93(65)	1.45e-4	0.25 $\pm$ 0.39	0.85 $\pm$ 0.73	2.13e-2	13(2)	4.60e-2
Photometric properties										
$s$	0.24 $\pm$ 0.34	0.07 $\pm$ 0.45	3.84e-2	32(6)	3.46e-3	1.20 $\pm$ 0.80	0.61 $\pm$ 0.66	2.88e-1	11(2)	5.90e-1
$C$	0.39 $\pm$ 0.59	0.05 $\pm$ 0.18	8.10e-3	72(26)	5.16e-1	1.05 $\pm$ 0.77	0.41 $\pm$ 0.61	2.12e-1	11(2)	6.83e-1
$s_{BV}$	0.39 $\pm$ 0.49	0.01 $\pm$ 0.30	4.80e-3	81(31)	1.98e-1	1.05 $\pm$ 0.94	0.91 $\pm$ 0.67	8.66e-1	6(0)	6.97e-1
$EBV$	0.51 $\pm$ 0.65	0.01 $\pm$ 0.15	4.10e-4	92(61)	4.23e-1	1.25 $\pm$ 0.64	0.21 $\pm$ 0.36	1.42e-3	70(22)	1.56e-1
$R_V$	0.24 $\pm$ 0.36	0.09 $\pm$ 0.49	3.95e-1	13(2)	1.04e-1	0.25 $\pm$ 0.40	1.42 $\pm$ 0.69	1.59e-3	92(61)	6.86e-1
$dBV_{60}$	0.13 $\pm$ 0.31	0.04 $\pm$ 0.23	9.74e-1	2(0)	6.00e-3	0.45 $\pm$ 0.57	0.84 $\pm$ 0.74	6.33e-1	1(0)	7.98e-3
$BV_{60}$	0.59 $\pm$ 0.46	-0.12 $\pm$ 0.13	1.02e-4	99(95)	7.61e-1	0.84 $\pm$ 0.58	0.05 $\pm$ 0.29	1.73e-2	22(4)	2.89e-1
Spectral properties										
$v_{\text{max}}$	0.27 $\pm$ 0.42	0.01 $\pm$ 0.29	2.58e-1	13(2)	6.32e-1	0.26 $\pm$ 0.49	1.30 $\pm$ 0.56	8.39e-3	79(30)	5.97e-1
$v_{\text{grad}}$	0.18 $\pm$ 0.42	0.06 $\pm$ 0.21	3.48e-1	4(0)	5.51e-1	0.85 $\pm$ 0.98	1.25 $\pm$ 0.99	6.48e-1	7(0)	4.89e-1
$v_{\text{neb}}$	0.59 $\pm$ 0.36	-0.01 $\pm$ 0.14	3.52e-2	12(2)	2.82e-1	1.24 $\pm$ 0.98	-0.23 $\pm$ 0.18	6.37e-3	6(0)	6.15e-1
Hubble residuals										
HR	0.15 $\pm$ 0.28	0.05 $\pm$ 0.17	1.40e-1	18(3)	1.02e-1	0.45 $\pm$ 0.59	0.41 $\pm$ 0.64	9.31e-1	2(0)	2.21e-3
$HR_L$	0.24 $\pm$ 0.35	0.01 $\pm$ 0.13	4.94e-3	78(29)	5.02e-1	0.45 $\pm$ 0.59	0.41 $\pm$ 0.64	9.76e-1	2(0)	4.10e-3
$HR_G$	0.19 $\pm$ 0.31	0.01 $\pm$ 0.13	1.22e-2	31(6)	1.72e-1	0.45 $\pm$ 0.59	0.41 $\pm$ 0.64	9.33e-1	2(0)	2.09e-2

**Notes.** Property, median and MAD EW(Å) of  $\text{Na I D}$  for the upper/lower half of the property sample, raw KS test and bootstrap probability (%) for the p-value $<0.05$  ( $<0.01$  in parentheses).

\* Raw KS test p-value between EW distributions divided by their median

† Bootstrap probability (%) of p-value $<0.05$  ( $<0.01$ ) between  $z$ -matched EW distributions divided by sweeping values within 40-60%

△ Multi-dimensional FF test p-value on the local environmental properties of the two EW samples

higher  $v_{\text{max}}$ <sup>1</sup> have larger EW) and the nebular velocity (higher receding velocities have larger EW). We show the cumulative distributions of EW divided according to  $R_V$  and to  $v_{\text{max}}$  for the old and young populations in Fig. 5. A relation of high-velocity SNe Ia with redder colours and lower  $R_V$  values had already been found (Wang et al. 2009; Foley & Kasen 2011). In App. B.2 we show that even after correcting the EW for the local SFR, the relations with SN properties are maintained.

The striking result that intrinsic SN properties, such as the ejecta or nebular velocities, correlate with properties of the intervening material, such as the  $\text{Na I D}$  EW, beyond local environmental characteristics, suggests that either sodium is a proxy for another physical property related to the explosion, or that the SN interacts with very nearby material in the line of sight. In asymmetric explosions, the central asymmetry, given by the nebular velocity, goes in the opposite direction of the outer material, shown by the photospheric velocities (Maeda et al. 2010; Maguire et al. 2018). In the framework of the DDet scenario, the first outer helium shell detonation propagates around the surface to the opposite side, leading to an off-centre second detonation (Townsley et al. 2019; Li et al. 2021). A core detonation observed from the initial ignition side will have ejecta moving at higher photospheric velocities, but preferentially redshifted receding nebular velocities.

### 3.3. Cluster analysis

In the previous section, we divided the SN Ia sample into two groups according to their local environments. However, this division was rather arbitrary and did not include SN properties, which may reveal clearer differences between real intrinsic populations. Furthermore, the posterior division into SN properties

was done by taking the median of each property, meaning that each new division could include different SNe. Instead of finding artificial one-dimensional divisions that are not realistic of true sub-populations of SNe Ia with possible overlapping properties, we use here a different approach consisting of clustering algorithms that consider all features of the sample, both intrinsic and environmental.

We use Gaussian Mixture Models (GMM, McLachlan & Peel 2000) that model the data through a probabilistic combination of Gaussians representing each subpopulation (see App. B.3 for details). In this clustering algorithm, the number of clusters is predetermined by the user. We use local environmental variables ( $\text{SFR}^L$  and  $t_{\text{age}}^L$ ) and SN properties ( $s$ ,  $R_V$  and  $v_{\text{max}}$ ) as input features to the GMM. Since we aim to study the differences in EW for various clusters, we omit in the clustering any narrow line information as well as any intrinsic property directly related to dust, such as colour (e.g.,  $C$ ,  $EBV$ ,  $BV_{60}$ ). Additional variables were also tested with similar results. However, as we increase the number of input features, the amount of SNe with available properties diminishes. These five properties result in 106 SNe Ia. The GMM algorithm provides the probability of each SN belonging to each cluster, and the largest probability provides the cluster membership. Additionally, we consider the uncertainties in the input parameters by doing a Monte Carlo that shifts the variables according to their covariance matrix and recalculates the probability of belonging to each cluster at each iteration. The final probability is the median of all simulations.

We first fix the number of clusters to two and find results similar to the previous section: environmental properties drive the separation between a young and an old component of SNe Ia, while SN properties play a very minor role in this separation. When using three clusters, the intrinsic properties emerge: there is one group of old SNe Ia, whereas the young group is now subdivided into two subpopulations, one with preferentially low

<sup>1</sup> In the table the  $\langle \text{EW}_{\text{lo}} \rangle$  for  $v_{\text{max}}$  refers to more negative velocities.

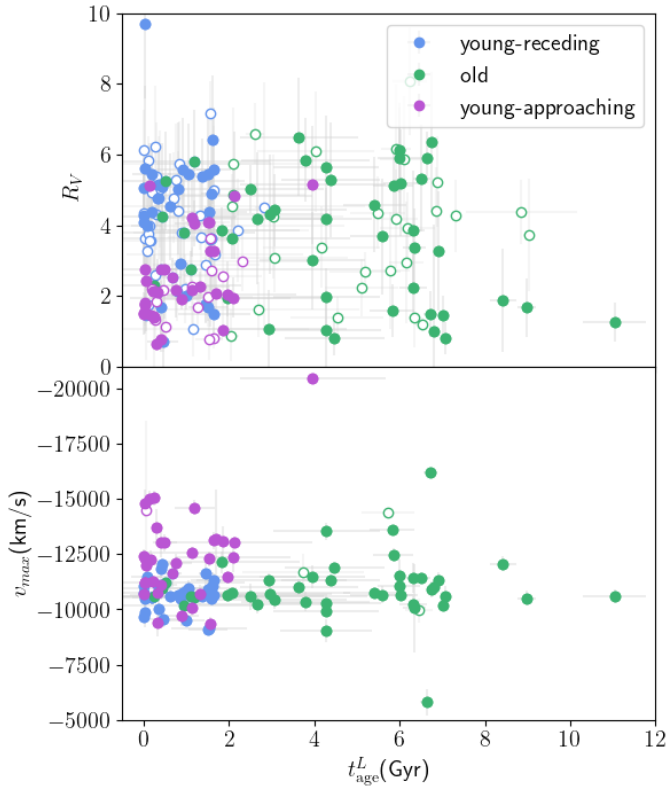


**Fig. 6.** Reddening law  $R_V$  and ejecta velocity  $v_{max}$  vs local age  $t_{age}^L$  (Gyr) for three clusters obtained through GMM: an "old" component (green), a "young-receding" (blue) and a "young-approaching" population (purple). Filled circles represent the initial SN sample, and open circles are SNe with one imputed variable.

**Table 6.** Median properties for three SN clusters: "old", "young-receding", and "young-approaching"

Property	Cluster		
	OLD	YOUNG-RECEDING	YOUNG-APPROACHING
Nr	44	29	33
EW	$-0.06 \pm 0.30$	$0.35 \pm 0.47$	$1.30 \pm 0.69$
VEL	$24 \pm 207$	$111 \pm 248$	$-67 \pm 221$
$\Delta\alpha$	$0.36 \pm 0.10$	$0.16 \pm 0.06$	$0.12 \pm 0.04$
<b>SFR<sup>L</sup></b>	$-5.08 \pm 1.02$	$-2.47 \pm 0.68$	$-2.41 \pm 0.87$
<b><math>t_{age}^L</math></b>	$4.43 \pm 2.45$	$0.82 \pm 0.61$	$0.49 \pm 0.47$
<b><math>s</math></b>	$0.87 \pm 0.09$	$0.91 \pm 0.15$	$0.98 \pm 0.05$
<b><math>C</math></b>	$0.07 \pm 0.09$	$0.06 \pm 0.11$	$0.24 \pm 0.24$
<b><math>s_{BV}</math></b>	$0.89 \pm 0.09$	$0.81 \pm 0.18$	$0.96 \pm 0.05$
<b><math>EBV</math></b>	$0.19 \pm 0.09$	$0.21 \pm 0.10$	$0.37 \pm 0.20$
<b><math>R_V</math></b>	$3.81 \pm 1.56$	$4.76 \pm 0.69$	$2.13 \pm 0.61$
<b><math>dBV_{60}</math></b>	$-0.011 \pm 0.001$	$-0.011 \pm 0.003$	$-0.013 \pm 0.003$
<b><math>BV_{60}</math></b>	$0.85 \pm 0.11$	$0.82 \pm 0.12$	$1.04 \pm 0.21$
<b><math>v_{max}</math></b>	$-10718 \pm 481$	$-10630 \pm 409$	$-12296 \pm 1008$
<b><math>v_{grad}</math></b>	$66.5 \pm 21.3$	$67.7 \pm 31.1$	$87.4 \pm 44.7$
<b><math>v_{neb}</math></b>	$-182 \pm 673$	$-482 \pm 1554$	$1427 \pm 974$
<b>HR</b>	$0.08 \pm 0.14$	$-0.01 \pm 0.09$	$-0.02 \pm 0.12$
<b><math>HR_L</math></b>	$0.06 \pm 0.15$	$0.04 \pm 0.09$	$0.00 \pm 0.12$
<b><math>HR_G</math></b>	$0.05 \pm 0.15$	$0.01 \pm 0.06$	$-0.04 \pm 0.13$

**Notes.** Property, median and MAD for three clusters: old, young-receding and young-approaching (see Tab. B.4 for the imputed sample). The five input properties used in the clustering are highlighted in bold.

$R_V$  and high  $v_{max}$  and another with higher  $R_V$  and lower  $v_{max}$  (see Fig. 6). Differences in other input features are less evident. Using four groups results roughly in the same clusters, plus a very small additional group of a few outlier members. We therefore stop at three clusters. The Akaike information criterion, which penalises additional parameters with an increasing number of clusters, confirms the three-member clustering.

Tab. 6 shows the median properties of all three groups that we dub "old", "young-receding" and "young-approaching" for reasons that will become clear later<sup>2</sup>. Besides the input parameters used for clustering, we also show the median of other SN properties, as well as the narrow line EW and velocities. To augment the sample, we also perform an imputation of missing data: SNe with four out of the five input parameters are imputed, and the new set is used to obtain a membership class. The extended imputed sample consists of 192 objects, and the statistics for this sample are also shown in Tab. B.4. The imputation is used only for labelling into a given cluster, but the statistics come from real measured data (see App. B.3 for details).

As expected, the old population has the lowest EW of Na I D mostly due to the different environment. We confirm that the two young populations have significant differences in EW that correlate with other extinction-related parameters such as the observed colour,  $EBV$  and  $R_V$ , but also to other properties such as the ejecta velocity, the velocity gradient and the nebular velocity. Compared to the receding population, the approaching sample has much stronger EW (1.30 vs 0.35 Å) as also shown in Fig. 7, larger extinction ( $EBV = 0.37$  vs 0.21), steeper reddening curves ( $R_V = 2.12$  vs 4.76), higher ejecta velocities ( $v_{max} = -12296$  vs  $-10630$  km s $^{-1}$ ), larger ejecta velocity gradients ( $v_{grad} = 87.4$  vs  $67.7$  km s $^{-1}$  d $^{-1}$ ) and higher redshifted nebular velocities ( $v_{neb} = 1427$  vs  $-482$  km s $^{-1}$ ). These findings are confirmed for the increased imputed sample.

In Fig. 8, we show the KS tests among the three clusters for various properties. These three clusters confirm that normal-velocity (NV) SNe Ia can be found in two groups ("old" and "young-receding"), whereas high-velocity (HV) objects form exclusively a different group ("young-approaching"), as found in Li et al. (2021). It is worth noting that Burns et al. (2014) also find evidence for a two-Gaussian mixture model for the fitted  $R_V$  parameter. Using their findings as an alternative prior to  $R_V$  only strengthens our results.

## 4. Discussion

In this section, we study the results in greater detail, in light of SN Ia models and findings of the literature.

### 4.1. Two populations

In Sect. 3.2, we divided the sample into two groups according to their local environment and, in Sect. 3.3, we found that a clustering analysis of two and three clusters recovers these two environmental populations. Such a division is not surprising and has been previously suggested in SN Ia studies as a prompt component and a delayed component (Mannucci et al. 2005; Sullivan et al. 2006). More recently, there has been evidence for two populations divided by the light-curve width parameter, which strongly correlates with the environment (Nicolas et al. 2021; Ginolini et al. 2025). In Fig. 9, we show the stretch distribution for the "old"

<sup>2</sup> The old population fully corresponds with the division of Sect. 4.1, i.e. they all have  $\log sSFR < 11.3$ , whereas the two young channels have over 60% of their environments with  $\log sSFR > 11.3$ .

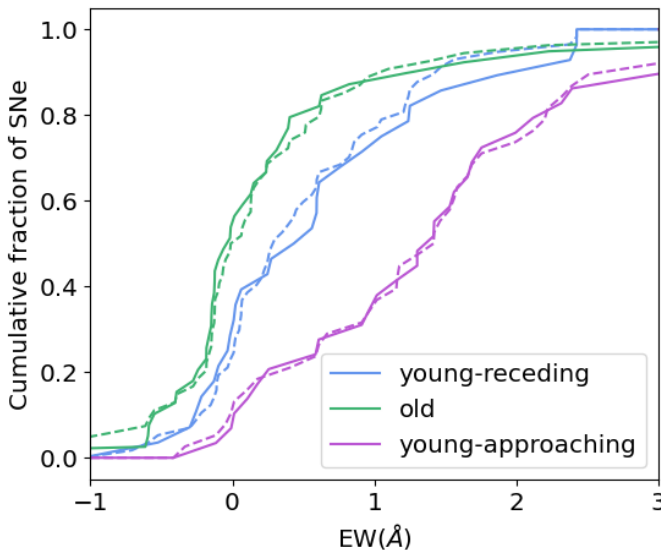


**Fig. 7.** Cumulative Na I D EW distribution for three clusters obtained through GMM: an "old" component (green), a "young-receding" (blue) and a "young-approaching" population (purple) for the normal (solid lines) and the imputed sample (dashed lines).

and "young" populations (both approaching and receding) found with our clustering. Although these two populations are distinct (KS p-value of 0.02, see Fig. 8) and the separation found in [Ginolin et al. \(2025\)](#) seems to isolate the majority of them, there is a clear overlap between the two. Fast-decliners (low stretch) SNe Ia can also be found in the old population, and slow-decliners (high stretch) in the young population.

More than a simple separation in light-curve width or in age of the entire SN Ia population, [Ginolin et al. \(2025\)](#) show that the brightness-stretch relation for their two stretch samples is significantly different (see their Fig. 7), which has profound implications in the powering mechanism of these two populations and therefore in their explosions and progenitors. In the left panel of Fig. 10, we show the SN magnitudes (corrected for distance and for the colour and mass-step calibrations) as a function of stretch ( $x_1$ ) for our two clusters. Fitting a line using LINMIX ([Kelly 2007](#)), we obtain different slopes for the two groups, although within the uncertainties ( $-0.072 \pm 0.043$  and  $0.166 \pm 0.033$  for the old and young populations, respectively, or a  $1.7\sigma$  difference).

[Polin et al. \(2019\)](#), see their Fig. 11) also argue that the SN Ia population could have two channels based on the relation of their brightness and ejecta velocity. We find slightly stronger differences in this parameter space (see right panel of Fig. 10) with the slopes of old and young samples differing in sign,  $(-8.88 \pm 5.99)$  and  $(6.70 \pm 4.27) \times 10^{-5} \text{ km s}^{-1}$  for the old and young populations, respectively, or a  $2.1\sigma$  difference. However, the fits are heavily dependent on a few higher-velocity objects. In the interpretation of [Polin et al. \(2019\)](#), there is a group of SNe Ia with no strong dependence of the brightness on Si II velocity, which corresponds to  $M_{\text{Ch}}$  explosion models, whereas the group of increasing brightness with velocity originates from sub- $M_{\text{Ch}}$  DDet explosions for which increasing WD mass (between 0.9 and 1.2  $M_{\odot}$ ) results in brighter (between -17.5 and -20.0 magnitudes) and faster ejecta (between 9500 and 16000  $\text{km s}^{-1}$ ). If our relations were to be confirmed with more data, the young channel would agree better with the sub- $M_{\text{Ch}}$  scenario.

In Tab. 5 we also see that the stretch within the old channel is still highly dependent on the environment (low  $FF_{\text{env}}$  of 3.5e-3), probably indicating that age may be a fundamental parameter

responsible for the variability of the old SNe Ia. The correlation between local age and stretch ( $-0.41$ , p-value of 0.005) confirms that younger SNe Ia have higher light-curve widths, as expected in the typical brightness-stretch relation ([Phillips 1993](#)). The young population, on the other hand, shows much less dependence of the stretch on environment ( $FF_{\text{env}}$  of 5.9e-1 and correlation with age of  $-0.28$ , p-value of 0.04), indicating that another mechanism may be at hand.

The age differences between both populations cannot be due to the cooling age of a WD, as this is inversely related to its mass, so that if the young population resulted from less massive sub- $M_{\text{Ch}}$  WDs, they should be older. This would mean that the age is determined by a younger companion rather than the WD itself. Although the normalised offset location was not used in the division nor the clustering, we find that both groups have significant differences: the old population has a median offset of 0.36 versus 0.16 for the young channel (KS test p-value of  $4.4e-9$  with  $P_{MC}=100\%$ ). This agrees with known age gradients due to the inside-out growth of galaxies (e.g., [Pérez et al. 2013](#)). The range of ages covered by the old population is larger than for the young population (see Tab. 4), and double-degenerate mergers can, in principle, explain such diversities better ([Maoz et al. 2014](#)).

Regarding the sodium absorption, it is clear that the young population encounters more gaseous material in the line of sight, as is expected in more star-forming regions. Indeed, there are clear differences between the two populations that remain related to the environment, e.g. both channels have stronger absorption closer to the centre of the hosts, although this seems again more important for the old population.

#### 4.2. Young asymmetric channel

In our study, the so-called young component of SNe Ia is further subdivided through clustering into two groups that seem to be related to explosion asymmetries through differences in the nebular velocity that also correlate with photospheric ejecta velocity and its gradient over time. This division separates SNe Ia into the known spectral categories ([Wang et al. 2009](#)) of normal velocity (NV) and high-velocity (HV) objects, whereas the old component is composed primarily of only NV SNe (see Tab. 6). Such a subdivision of the NV group into two further groups has already been pointed out ([Kawabata et al. 2020](#); [Li et al. 2021](#)). As this HV group preferentially happens for the young channel, which is more centrally located (see Tab. 6), the observed preference for HV closer to the centre of galaxies is confirmed ([Wang et al. 2013](#); [Pan 2020](#); [Nugent et al. 2023](#)).

HV SNe Ia have preferentially redshifted nebular velocities corresponding to asymmetric central explosions moving away from the observer, whereas NV SNe Ia present more blueshifted nebular velocities moving towards the observer. These observations can be explained in the light of the DDet explosion mechanism, in which a sub- $M_{\text{Ch}}$  WD has an outer helium layer that detonates and creates a supersonic wave propagating on the surface and coinciding on the opposite side to trigger a secondary off-centre carbon-oxygen detonation (e.g., [Nomoto 1982](#); [Hoeftlich et al. 1996](#); [Woosley & Kasen 2011](#); [Shen & Moore 2014](#); [Polin et al. 2019](#)). [Townsley et al. \(2019\)](#), see their fig. 4) demonstrate with multi-dimensional simulations that the Si II velocity is more blueshifted when the first detonation is viewed face-on: depending on the viewing angle, the ejecta velocity can change from  $9000 \text{ km s}^{-1}$  when viewed from the opposite side to  $17000 \text{ km s}^{-1}$  when viewed from the same side (see their Fig. 4). This arises because the core detonation is less curved and stronger as

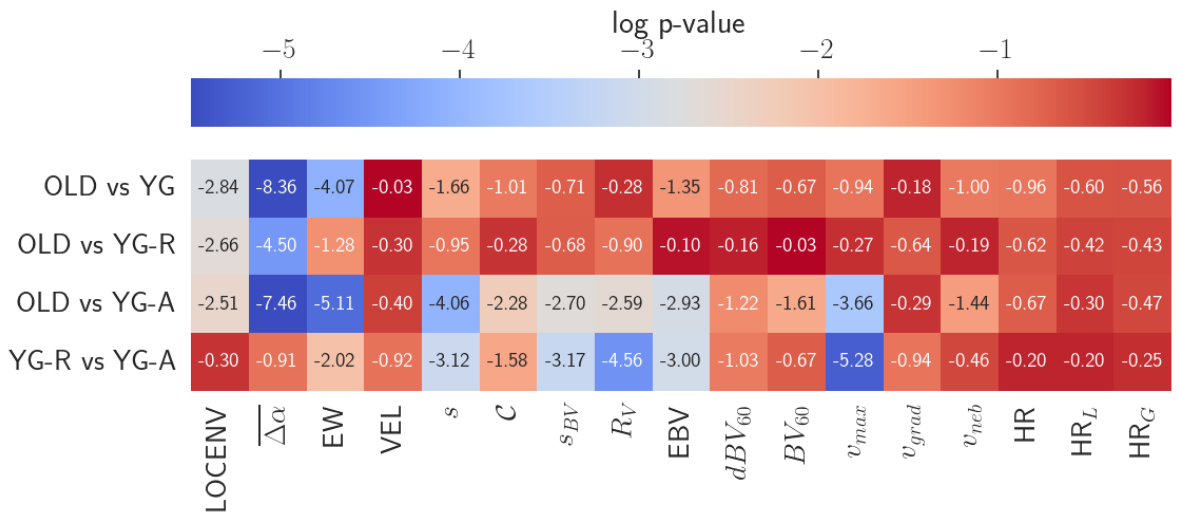


**Fig. 8.** KS test p-values for different properties divided according to three clusters: "old" (OLD), "young-receding" (YG-R) and "young-approaching" (YG-A). The first row joins both young groups into a single one (YG). "LOCENV" refers to a combination of local environmental properties ( $sSFR^L$ ,  $SFR^L$ ,  $t_{age}^L$ ,  $A_V^L$  and  $M_*^L$ ) through a FF test. For reference, a p-value of 0.05 corresponds to  $\log(p\text{-val}) = -1.30$ .

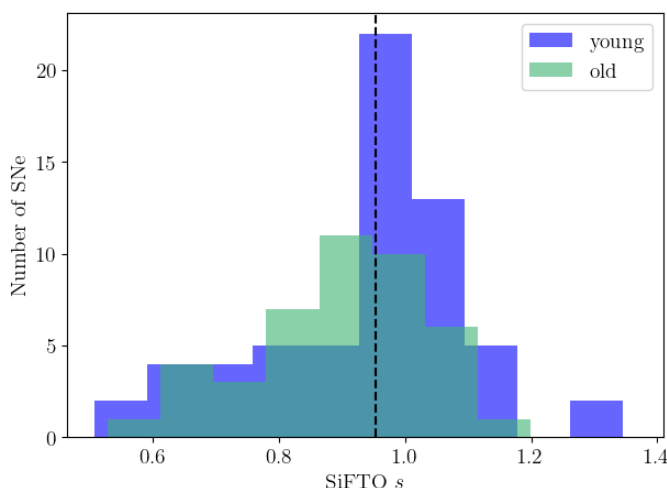


**Fig. 9.** SiFTO stretch distribution for the old and young (both receding and approaching) components obtained with the GMM clustering. The vertical dashed line is the division value of  $s = 0.954$  ( $x_1 = -0.48$ ) from [Ginolini et al. \(2025\)](#), which is close to the median of the entire sample ( $< s > = 0.959$ ).

it reaches the surface. This has been confirmed in other multi-dimensional simulations ([Holas et al. 2025](#)).

The sample of young-approaching SNe Ia has thus larger ejecta velocities and more redshifted nebular velocities than the young-receding population, in agreement with the sub- $M_{\text{Ch}}$  DDet scenario. We also find that the young-approaching objects have slightly higher stretch ( $< s_{YG-A} > = 0.98$  vs  $< s_{YG-R} > = 0.91$ , see Tab. 6) and are more luminous (see right Fig. 10). Sub-Chandrasekhar explosion models do show a relation between stretch, magnitude and viewing angle; however, this relation often goes in the opposite direction: surface He detonations viewed face-on are fainter and shorter-lived ([Townsley et al. 2019](#); [Collins et al. 2025](#)). Nonetheless, in the edge-lit scenario, in which the core ignition is triggered between the core and the shell right after the He detonation ([Livne & Glasner 1990](#)), the explosions with initial surface detonations on the side of the observer are brighter and longer-lived ([Gronow et al. 2021](#)). However, this scenario would not explain the redshifted nebular velocities since

both detonations happen on the same side. In general, a relation between  $v_{max}$ , stretch and brightness is expected in the sub- $M_{\text{Ch}}$  scenarios, but the strength of this relation and its dependences on WD mass, viewing angle, and offset from the core ([Holas et al. 2025](#)) vary among studies. We caution that other asymmetric SN Ia scenarios exist (e.g., [Pollin et al. 2025](#)). Finally, it is also possible that there exist two different populations in similar environments, i.e. that the approaching and receding groups have distinct progenitor or explosion mechanisms.

#### 4.3. Nearby material

The EW of the Na I D absorption lines in SNe Ia is related to the intervening material in the line of sight. The old population has less star formation and cleaner environments, so they have lower EW than the young channel, as one would expect. On the other hand, the young-approaching and young-receding groups have strong differences in sodium absorption that are seemingly not related to environments. This is accompanied by strong differences in observed colours and varying reddening laws: young-approaching SNe Ia are redder, they have steeper reddening curves and present stronger sodium absorption. Moreover, although the significance is lower, the young-approaching sample has more blueshifted sodium lines, indicating gas movement towards the observer (see Tab. 6).

In Fig. 11, we show the EW of sodium compared to the  $EBV$  values from SNooPy for the three clusters found. For comparison, the relation obtained by [Poznanski et al. \(2012\)](#) is shown in orange. Although there are caveats to using low-resolution spectra to estimate extinction ([Poznanski et al. 2011](#)) and there is a lot of scatter, it is interesting to see a higher fraction of young-approaching SNe Ia above the line (51% are above and 38% above  $1\sigma$  of their uncertainty) compared to the other two groups (the old group has 10% above and 8% above  $1\sigma$ , and the young-receding has 21% above and 11% above  $1\sigma$ ). This indicates that there is an excess of sodium absorption for the approaching group. [Phillips et al. \(2013\)](#) found that indeed some SNe Ia presented stronger sodium absorption than expected from a calibration of the MW, and that these excess objects had in fact blueshifted absorption. This agrees well with the sample of young-approaching SNe, which are also more blueshifted on average.

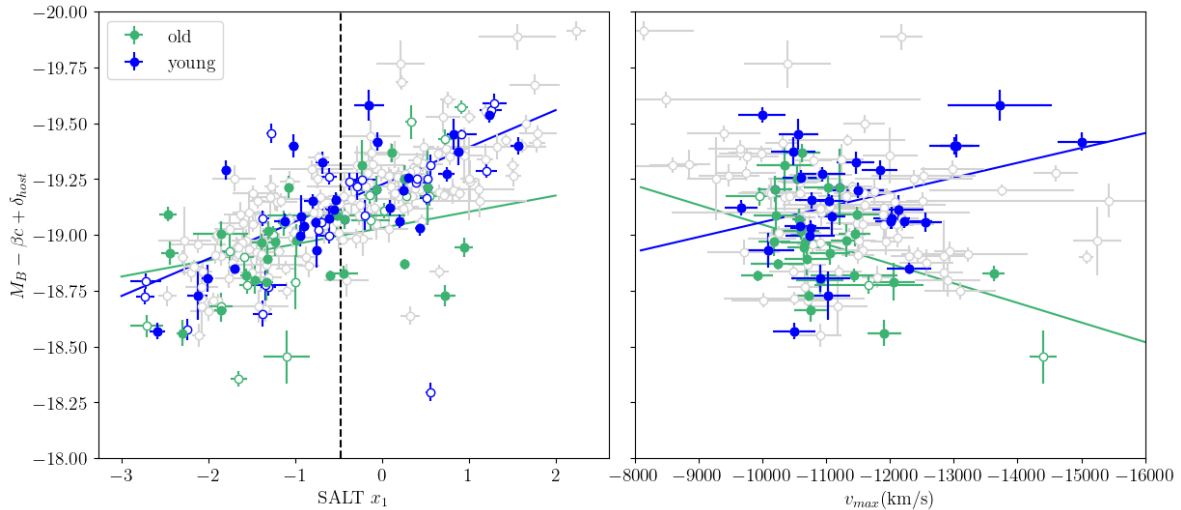


**Fig. 10.** Absolute magnitude corrected for colour (and mass-step) versus SALT  $x_1$  (left) and Si II ejecta velocity (right) for the old (green) and young (blue) components obtained with GMM clustering (open coloured circles for the imputed sample). Grey open dots are objects without cluster membership.

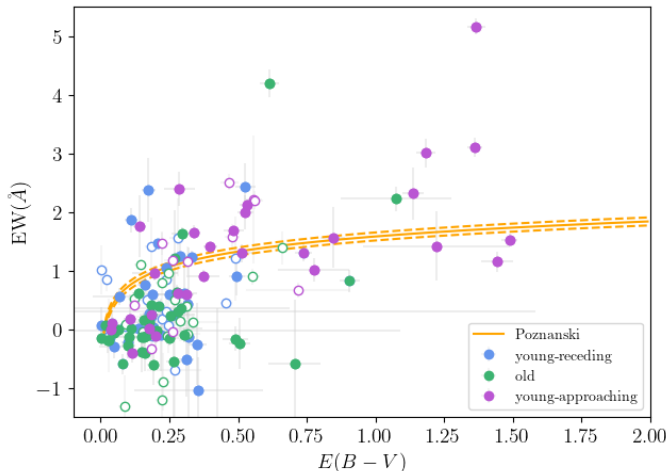


**Fig. 11.** Na I D EW vs  $E(B - V)$  for SNe Ia divided according to the three clusters for the initial sample (filled circles) and the imputed sample (open circles). The Poznanski relation is shown in orange.

HV objects, belonging mostly to the young-approaching sample, have been associated with redder colours before (Foley & Kasen 2011) and to lower  $R_V$  values (Wang et al. 2009). Intrinsic colour differences not captured in the stretch-dependent intrinsic colours of SNOoPy could affect the reddening estimates, as suggested by Polin et al. (2019); however, the accompanying strong differences in Na I D absorption argue for real dust differences. The line-of-sight material responsible for these differences is more local than our  $r = 0.5$  kpc host apertures around the SNe, and more strikingly, is related to intrinsic explosion properties such as the ejecta velocity and the nebular shifts. The most plausible explanation is that the SN interacts with material that is present in its vicinity, with explosion asymmetries and viewing angle effects possibly related to this interaction and its strength.

At later times (30-90 days after maximum), Förster et al. (2013) claim that sodium absorption differs according to the  $B - V$  evolution. In this study, we only find mild indications for this (KS p-value of 0.09 between young-approaching and young-receding), and it would seem that the diversity of this decay has a stronger relation to some property of the environment (see FF<sub>env</sub> in Tab. 5). It is also worth mentioning that Wang et al. (2019)

find late-time blue-excess (60-100 days past maximum) for HV objects, and they interpret this as evidence for light-echoes from very nearby material, in agreement with our findings.

Two main alternatives for the nearby material have been debated in the literature: CSM ejected from the progenitor system prior to explosion ( $\lesssim 1$  pc from the SN), and nearby dust clouds from the ISM ( $> 1$  pc). The following evidence further argues for nearby material around SNe Ia, and we highlight why the ISM interpretation is preferred: i) light-echoes in SNe Ia are known to exist (e.g., Wang et al. 2008; Crotts & Yourdon 2008; Yang et al. 2017), yet only for a few SNe and the inferred distances for the dust are larger than 10 pc; ii) peculiar steep reddening curves (low  $R_V$ ) in SNe Ia, especially for HV objects as mentioned before, are best explained by normal dust (Burns et al. 2014; Marino et al. 2015) rather than for a CSM-like material (Goobar 2008); iii) time-evolution in  $EBV$  and  $R_V$  (e.g., Förster et al. 2013) are well modeled by scattering of dust located at distances larger than  $> 1$  pc for most SNe Ia (Bulla et al. 2018); iv) time-varying narrow lines such as sodium or potassium occur only in some SNe Ia with high-resolution spectra (Patat et al. 2007; Simon et al. 2009; Graham et al. 2015), whereas statistical low-resolution sample do not show ubiquitous variation (Paper I), this is consistent with geometrical effects from dust clouds in a patchy ISM affecting only some objects (see also Maeda et al. 2016); v) excess blueshifts in narrow features of sodium (Sternberg et al. 2011; Clark et al. 2021) associated to additional absorption (Maguire et al. 2013; Phillips et al. 2013) can be explained by mass-loss episodes prior to explosion in the CSM scenario, but they can also arise from acceleration of ISM dust clouds due to the SN radiation (Hoang 2017).

Another line of evidence that argues for ISM is the lack of time-evolving polarisation in SNe Ia (Kawabata et al. 2014; Patat et al. 2015; Nagao et al. 2018, although see Yang et al. 2018). Moreover, the increased continuum polarisation (and its bluer peak) in SNe Ia occur preferentially in arms of spiral galaxies and closer to the centre (Zelaya et al. 2017; Chu et al. 2022), arguing for increased IS dust. Indeed, one of the leading arguments against CSM has been the location of those SNe Ia with signatures of nearby material: they are always in central, star-forming, dusty regions, agreeing with an IS origin. We confirm that this is the case for the young-approaching channel, which has more intervening material. But the young-receding channel

has indeed almost the same environments and suffers from much less extinction. So, the signatures of nearby material go beyond environments, and there could be a coincidence of effects: the progenitors of the young dusty channel could eject CSM that is only viewed on certain angles. Nonetheless, we focus in the next section on the ISM interpretation.

#### 4.4. Grain disruption by SN radiation

SN radiation can interact with nearby IS dust clouds and alter the dust size distribution responsible for the  $R_V$  via a) dust sublimation, but the radius ( $< 0.2\text{pc}$ ) where this occurs is too small (Waxman & Draine 2000; Hoang et al. 2019), b) cloud-cloud collisions (Hoang 2017), but the duration for grain shattering ( $\sim 100$  yr) is too long (Hoang et al. 2019), and c) radiative torques that generate centrifugal forces leading to dust disruption (Hoang et al. 2019; Giang et al. 2020). The latter two processes are particularly interesting because they can also release sodium and other species trapped in dust grains (dust depletion, see e.g., Field 1974; Konstantopoulou et al. 2022) back into the gas-phase. In such cases, sodium abundance is increased without a corresponding increase in extinction, as is observed for the young-approaching sample (Fig. 11). Moreover, in a patchy ISM, multiple cloud components can increase the EW of sodium without an increase in extinction (Maxted 2025).

In the asymmetric sub- $M_{\text{Ch}}$  DDet scenario, the events with initial surface detonations facing the observer correspond to our group of young-approaching objects. These also have higher extinction and stronger Na I D EW absorption. If radiative torques from the SN radiation are responsible for disrupting the grains, shifting their sizes (and  $R_V$ ) and making sodium more abundant, then that SN group needs to have an additional early source of radiation capable of imprinting that extra radiation pressure that, by maximum light, has already changed the grain distribution. In principle, the helium burning in the outer shell of the WD could provide the additional radiation at early times, or even shocks from the collision between the CO detonation and the He detonation (Piro & Nakar 2025). In fact, some SNe Ia do show signs of early emission (e.g., Marion et al. 2016; Hosseinzadeh et al. 2017; Dimitriadis et al. 2019; Ni et al. 2023) with variations in their early-time light-curves and colours (Bulla et al. 2020; Han et al. 2020), possibly making up two groups that relate to ejecta velocities (Stritzinger et al. 2018). Interestingly, Ni et al. (2025) recently provided evidence for three populations based on early colours, whereby one population would come from old environments, and the two others have more similar young environments.

The radiation pressure of strong radiation fields of bolometric luminosity,  $L_{\text{bol}}$ , and effective wavelength,  $\lambda_{\text{eff}}$ , can accelerate nearby clouds with grains of size,  $a$ , located at distance,  $d$ , to terminal velocities,  $v$ , of:

$$v \simeq 171 \left( \frac{L_{\text{bol}}}{10^8 L_{\odot}} \right)^{1/2} \left( \frac{d}{100\text{pc}} \right)^{-1/2} \left( \frac{a}{10^{-5}\text{cm}} \right)^{-1/2} \frac{\text{km}}{\text{s}}. \quad (1)$$

The bolometric luminosity of the early excess He detonation depends on the WD mass and the He layer mass (Polin et al. 2019), but it can reach  $10^8 L_{\odot}$  to imprint  $\sim 100 \text{ km s}^{-1}$  to the clouds, as has been measured for the Na I D blueshifts.

Additionally, the radiative torque (RAT) model predicts that the irregular grains can be spun to fast angular speeds,  $\omega$ , as follows:

$$\omega = A \left( \frac{a}{10^{-5}\text{cm}} \right)^n \left( \frac{\lambda_{\text{eff}}}{5\mu\text{m}} \right)^{-1.7} \left( \frac{L_{\text{bol}}}{10^9 L_{\odot}} e^{-\tau} \right)^{1/3} \left( \frac{d}{\text{pc}} \right)^{-2/3} \frac{\text{rad}}{\text{s}}, \quad (2)$$

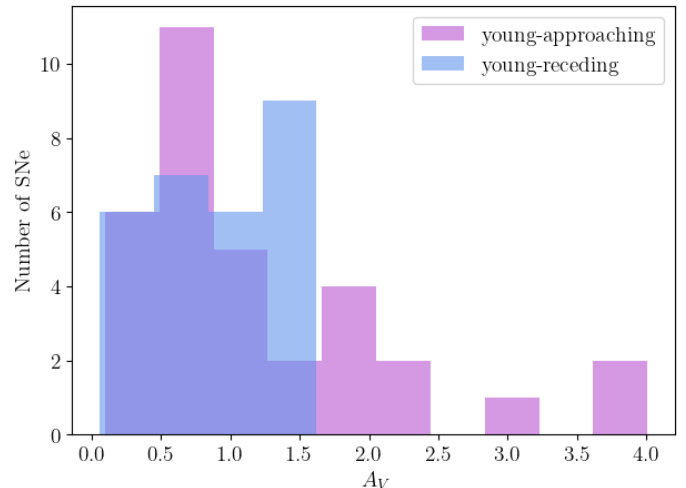
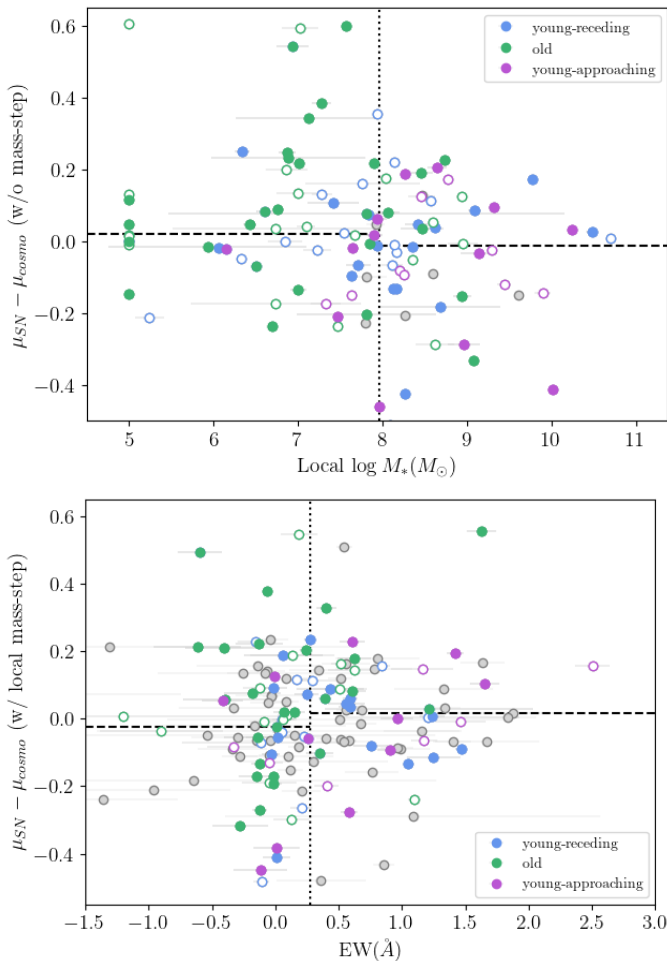


Fig. 12.  $A_V$  distributions for SNe Ia in the young-receding and young-approaching groups.

where  $A$  and  $n$  depend on the wavelength and grain size (see Hoang et al. 2019). For a SN, the evolution of the emission needs to be solved to obtain  $\omega(t)$ . The centrifugal forces created by the spin-up can tear the grains apart if they exceed a critical rotation of  $\omega_{\text{disr}} = \frac{2}{a} \left( \frac{S_{\text{max}}}{\rho} \right)^{1/2}$ , where  $\rho$  is the grain mass density and  $S_{\text{max}}$  is the maximum tensile strength of the grain, which is rather uncertain for dust. Giang et al. (2020) show that grains with maximum tensile values between  $10^7 - 10^{10} \text{ erg cm}^{-3}$  can be disrupted 10 to 40 days from explosion for clouds at  $d = 1 \text{ pc}$  due to the SN radiation alone. Excess emission from the surface detonation can destroy them earlier and at larger distances. Interestingly, maximum tensile strengths decrease for larger, composite grains, i.e. those that are easier to disintegrate. This means that grains that have metal species attached are possibly easier to destroy, and the fraction of excess sodium SNe Ia should, in principle, be higher than the fraction of low- $R_V$  SNe Ia. Taking our young-approaching sample, we measure a fraction of 67% of SNe with  $R_V$  values lower than 2.6, which is the lower limit of the MW range. This fraction is higher than the objects with excess sodium (51%), but the statistics are too low to draw firm conclusions.

One problem of the RAT disruption model in the form presented in Hoang et al. (2019) and Giang et al. (2020), is that all SNe Ia would end up sooner or later disrupting grains (even without early emission), and even core-collapse SNe (CC-SNe) would as well. The evidence for nearby material in SNe Ia comprises only a fraction of them, and not all CC-SNe show evidence of intervening matter. In fact, some CC-SNe seem to have surprisingly less sodium absorption than expected given their star-forming environments (Paper III). Given the uncertainty in some of the model parameters, particularly the tensile strength, there is room for improvement.

Another important consideration in the RAT disruption model is that the dust mass around the young population (approaching and receding) should be, on average, equal because of its ISM origin. This implies that the additional redder colours seen in the young-approaching objects should be explained solely by changes in the extinction curve and dust scattering, without changing the amount of dust mass. Qualitatively, this could be explained through dust grains becoming smaller (from  $R_V$  of 3.1 to 1.5), and preferentially absorbing and scattering wavelengths closer to  $B$  and  $V$ . In fact, Giang et al. (2020, see their figs. 3 and 4) present this change in the extinction curve for several cloud



**Fig. 13.** *Upper:* HR without mass-step as a function of local stellar mass. *Lower:* HR with local mass-step correction as a function of Na I D EW. The three GMM clusters are shown in colours for the initial (filled) and imputed samples (open). Median of the entire population is shown as vertical dotted lines. The horizontal dashed lines indicate the median of the HR for low and high EW or mass values, respectively.

distances and tensile strengths, assuming dust mass conservation and predicting in all cases that  $A_\lambda$  augments at  $\lambda < 0.4\mu\text{m}$  while it decreases at  $\lambda > 0.4\mu\text{m}$ . At the wavelength of V-band, comparing the median value of the young-receding population of  $\langle A_V \rangle = \langle R_V \rangle \times \langle EBV \rangle = 1.0$  with that of the young-approaching  $\langle A_V \rangle = 0.79$ , we see that it consistently decreases; however, for the most extinguished objects, there does not seem to be equivalents with higher extinction in the young-receding population (see Fig. 12). This poses a problem for the RAT disruption interstellar origin of the material under the assumptions of Giang et al. (2020). We note that the scattering effect for which bluer light from earlier epochs of the SN is scattered by the dust into the line of sight would only decrease  $EBV$  (and increase  $R_V$  with mostly constant  $A_V$ <sup>3</sup>) of the approaching SNe Ia, unable to explain this discrepancy.

#### 4.5. Cosmological mass-step

The mass-step in SN Ia cosmology is the third calibration correction, and it depends on the host environment. Its origin is actively debated in the literature with claims for an extrinsic dust origin, an intrinsic SN difference or a combination of both (e.g.,

Johansson et al. 2021; Thorp et al. 2021; Meldorf et al. 2023; Popovic et al. 2024). In the light of the current study, if the young and old channels are really two independent SN populations with possible different powering mechanisms, then the first  $\alpha$  brightness-stretch calibration could be different (see Sect. 3.2), affecting the calibration (Ginolini et al. 2025). If we assume that these two populations have the same Phillips relation apt for calibration, then we arrive at the  $\beta$  brightness-colour correction that is composed of an intrinsic colour and a dust extinction factor. Let us suppose that the intrinsic colours and their relation to intrinsic luminosity are equal for all SN Ia groups. Moreover, let us assume that reddening and absorption due to dust follow the exact same linear relation as the intrinsic colour-brightness relation. Under these assumptions, we still have the problem of a varying amount of dust: the young population, particularly the approaching one, suffers from more dust absorption in  $B$  and  $V$  bands than the old sample. This is a principle, not an issue, since this second colour calibration would take that into account. However,  $\beta \simeq R_V + 1$  and we show that  $R_V$  changes substantially for the two young sub-samples, invalidating therefore the calibration. To exacerbate things, dust scattering and echoes from this nearby material (present especially in young-approaching SNe Ia) can add blue light from earlier emission into the maximum SN light, depending on the geometry and distance of the clouds (Bulla et al. 2018), going exactly in the opposite direction of the reddening-extinction relation. So, even in the most optimistic scenarios that fulfil many of our assumptions, the simplistic SN Ia calibration seems unreasonable and dangerous for a large and heterogeneous population. Multiple channels for SNe Ia can have important implications for cosmological constraints (e.g., Wojtak & Hjorth 2025; Martins et al. 2025)

A third calibration may, in fact compensating over-corrections to some populations from the other two calibrations. In upper Fig. 13, we show the HR (without mass-step correction) as a function of the local stellar mass. We can see that the low-mass objects on the left make up mostly the old population, whereas the high-mass objects correspond to the young population. In that sense, the mass-step would be naturally explained as a split of two populations that have intrinsic differences (e.g., in asymmetries) but also significantly different environments such as age and dust. These findings agree with studies showing that the mass-step is a result of local differences such as stellar age (Rose et al. 2019; Rigault et al. 2020). In a recent work, Burgaz et al. (2025) show that NV have a strong mass-step, while for HV objects it is consistent with zero. If NV are indeed partly split into the old and young components, this is consistent with our results: NV would have two intrinsic populations that the mass-step picks up. If HV objects are part of a single population, on the other hand, then it also makes sense that they have less scatter in the HR (Wang et al. 2009). Toy et al. (2025) also find that the mass-step in the outskirts is reduced with respect to the central parts of the galaxies. As a single channel, the old population is preferentially located in the outskirts, while in the centre we have the two young populations with differing dust properties, so it makes sense that no mass-step is present for a single homogeneous old and outer population. However, a strong mass-step in the inner region means a relation to mass and environment. We confirm in Tab. 5 that two HR distributions within the young population have a strong environmental dependence ( $FF_{\text{env}} \sim 1\text{e-}3$ ) unrelated to dust (no EW difference), perhaps indicating changes in intrinsic luminosity for different progenitor ages, e.g., different WD mass in the sub- $M_{\text{Ch}}$  scenario (see Sect. 4.1).

In Tab. 3 we find that the EW distributions change according to Hubble residuals. The difference is stronger for HR after

<sup>3</sup> Private communication with M. Bulla

the local mass-step correction. In Fig. 13 we show the HR as a function of EW, and we highlight the median differences between low-EW and high-EW objects (below and above  $\langle \text{EW} \rangle = 0.203$ ). This division by the median separates most of the old (with low EW) from the young (with high EW) population. It indicates that even though the mass-step correction was included, the young population is fainter after all other corrections. By correcting with a higher assumed  $\beta$  (i.e. a higher  $R_V$ ) we over-correct the young-approaching population that ends up being fainter. Some of the SNe with the highest EW and HR in the figure are indeed from the approaching sample. However, we do not see in Tab. 6 that the young-approaching HR are significantly fainter than the young-receding, as one would expect under this hypothesis. Larger samples will shed more light on this.

Finally, although a fourth standardisation correction could be included to further diminish HR based on the EW, we strongly advocate not to do this and rather focus on well-understood homogeneous sub-populations of SNe Ia for cosmology.

## 5. Conclusions

In this work, we have analysed the EW and VEL of the narrow Na I D absorption with respect to a variety of properties from the hosts and the SNe, both photometric and spectroscopic. Our main conclusions are:

- The largest driver of the strength of sodium in the line of sight of SNe Ia is the environment: SNe in young, star-forming, central regions have significantly more sodium than their counterpart.
- The observed colours at maximum and at late times (60 days post maximum), as well as the colour excess of SNe Ia, are strongly related to Na I D abundance, showing that it is a good tracer of extinction. The light-curve width parameters are also significantly different according to the EW, which is expected given their environmental dependence.
- Nebular velocities are strongly related to EW of Na I D showing that there is a relation between intrinsic SN properties and the gas and dust in the line of sight.
- We find an optimal environmental division between two SN Ia samples (based on sSFR) and show that the young sample has important differences in the EW of Na I D when divided according to colours, colour excess,  $R_V$ , silicon ejecta velocity, silicon velocity gradient, and nebular velocity. This strengthens the idea that within the same young local environment, intrinsic SN properties affect or are affected by the intervening material.
- The young-approaching channel of SNe Ia, besides being composed of HV objects with low  $R_V$  and high extinction in the  $V$  band, is also consistent with more blueshifted Na I D lines and excess absorption with respect to what is expected from its extinction.
- We provide a possible interpretation of these results in which the young population comes from an asymmetric explosion that interacts with nearby material. In the sub- $M_{\text{Ch}}$  DDet, for example, early emission on the side of the first detonation could imprint additional radiation that pushes nearby ISM clouds and spins up dust grains through radiation torques, disrupting them, lowering the size distribution ( $R_V$ ) and releasing metals trapped in grains to the gas-phase. Nonetheless, details of this scenario need to be properly addressed, e.g. how and when the disruption occurs and why it affects only a fraction of SNe Ia, or why there seem to be deviations in the expected  $A_V$  distributions for two orientations of the

young populations subject to the same amount of ISM dust mass.

- The local mass-step in cosmology can be explained through these two, old and young, populations occurring in different mass regimes, as well as in different offsets from the galaxy centres. Aside from differences between the two populations in intrinsic properties, such as luminosity, colour and the luminosity-stretch and colour relations, one of the populations has clearly a fraction of SNe Ia with lower  $R_V$  (the young-approaching) that, when corrected with a single higher  $\beta$  parameter, get fainter after standardisation.

This work provides further light into the SN Ia puzzle, showing that these objects are complex and heterogeneous, that the intrinsic properties are related to nearby material, and that cosmological standardisation should be carefully revisited.

**Acknowledgements.** We acknowledge the financial support from the María de Maeztu Thematic Core at ICE-CSIC. C.P.G. acknowledges financial support from the Secretary of Universities and Research (Government of Catalonia) and by the Horizon 2020 Research and Innovation Programme of the European Union under the Marie Skłodowska-Curie and the Beatriu de Pinós 2021 BP 00168 programme. C.P.G. and L.G. recognise the support from the Spanish Ministerio de Ciencia e Innovación (MCIN) and the Agencia Estatal de Investigación (AEI) 10.13039/501100011033 under the PID2023-151307NB-I00 SNNEXT project, from Centro Superior de Investigaciones Científicas (CSIC) under the PIE project 20215AT016 and the program Unidad de Excelencia María de Maeztu CEX2020-001058-M, and from the Departament de Recerca i Universitats de la Generalitat de Catalunya through the 2021-SGR-01270 grant. J. D., R. S. and G. M. acknowledge support by FCT for CENTRA through the Project No. UID/99/2025. J. D. also acknowledges support by FCT under the PhD grant 2023.01333.BD, with DOI <https://doi.org/10.54499/2023.01333.BD>. This research has made use of the PYTHON packages ASTROPY (Astropy Collaboration et al. 2013, 2018, 2022), NUMPY (Harris et al. 2020), MATPLOTLIB (Hunter 2007), SCIPY (Virtanen et al. 2020), PANDAS (The pandas development team 2020; Wes McKinney 2010).

## References

Anderson, J. P., James, P. A., Förster, F., et al. 2015, MNRAS, 448, 732  
 Astropy Collaboration, Price-Whelan, A. M., Lim, P. L., et al. 2022, ApJ, 935, 167  
 Astropy Collaboration, Price-Whelan, A. M., Sipócz, B. M., et al. 2018, AJ, 156, 123  
 Astropy Collaboration, Robitaille, T. P., Tollerud, E. J., et al. 2013, A&A, 558, A33  
 Benetti, S., Cappellaro, E., Mazzali, P. A., et al. 2005, ApJ, 623, 1011  
 Bildsten, L., Shen, K. J., Weinberg, N. N., & Nelemans, G. 2007, ApJ, 662, L95  
 Blondin, S., Matheson, T., Kirshner, R. P., et al. 2012, AJ, 143, 126  
 Blondin, S., Prieto, J. L., Patat, F., et al. 2009, ApJ, 693, 207  
 Bloom, J. S., Kasen, D., Shen, K. J., et al. 2012, ApJ, 744, L17  
 Branch, D., Dang, L. C., Hall, N., et al. 2006, PASP, 118, 560  
 Brout, D. & Scolnic, D. 2021, ApJ, 909, 26  
 Brout, D., Scolnic, D., Popovic, B., et al. 2022a, ApJ, 938, 110  
 Brout, D., Taylor, G., Scolnic, D., et al. 2022b, ApJ, 938, 111  
 Bulla, M., Goobar, A., & Dhawan, S. 2018, MNRAS, 479, 3663  
 Bulla, M., Miller, A. A., Yao, Y., et al. 2020, ApJ, 902, 48  
 Burgaz, U., Maguire, K., Galbany, L., et al. 2025, arXiv e-prints, arXiv:2509.02687  
 Burns, C. R., Stritzinger, M., Phillips, M. M., et al. 2014, ApJ, 789, 32  
 Cardelli, J. A., Clayton, G. C., & Mathis, J. S. 1989, ApJ, 345, 245  
 Cavichia, O., Mollá, M., Bazán, J. J., et al. 2024, MNRAS, 532, 2331  
 Chu, M. R., Cikota, A., Baade, D., et al. 2022, MNRAS, 509, 6028  
 Cikota, A., Hoeflich, P., Baade, D., et al. 2026, ApJ, 996, L10  
 Clark, P., Maguire, K., Bulla, M., et al. 2021, MNRAS, 507, 4367  
 Collins, C. E., Shingles, L. J., Sim, S. A., et al. 2025, MNRAS, 538, 1289  
 Conley, A., Guy, J., Sullivan, M., et al. 2011, ApJS, 192, 1  
 Conley, A., Sullivan, M., Hsiao, E. Y., et al. 2008, ApJ, 681, 482  
 Crotts, A. P. S. & Yourdon, D. 2008, ApJ, 689, 1186  
 Dempster, A. P. et al. 1977, Journal of the Royal Statistical Society. Series B (Methodological), 39, 1  
 DES Collaboration, Abbott, T. M. C., Acevedo, M., et al. 2024, ApJ, 973, L14  
 Dhawan, S., Leibundgut, B., Spyromilio, J., & Blondin, S. 2017, A&A, 602, A118  
 Dilday, B., Howell, D. A., Cenko, S. B., et al. 2012, Science, 337, 942

Dimitriadis, G., Foley, R. J., Rest, A., et al. 2019, *ApJ*, 870, L1

Drozdov, D. 2016, PhD thesis, Clemson University, South Carolina

Duarte, J., González-Gaitán, S., Mourão, A., et al. 2023, *A&A*, 680, A56

Duarte, J., González-Gaitán, S., Mourão, A., et al. 2025, *A&A*, 700, A169

Fasano, G. & Franceschini, A. 1987, *Monthly Notices of the Royal Astronomical Society*, 225, 155

Ferretti, R., Amanullah, R., Goobar, A., et al. 2016, *A&A*, 592, A40

Field, G. B. 1974, *ApJ*, 187, 453

Filippenko, A. V., Richmond, M. W., Branch, D., et al. 1992, *AJ*, 104, 1543

Fitzpatrick, E. L. 1999, *PASP*, 111, 63

Folatelli, G., Morrell, N., Phillips, M. M., et al. 2013, *ApJ*, 773, 53

Foley, R. J., Fox, O. D., McCully, C., et al. 2014, *MNRAS*, 443, 2887

Foley, R. J. & Kasen, D. 2011, *ApJ*, 729, 55

Foreman-Mackey, D., Hogg, D. W., Lang, D., & Goodman, J. 2013, *PASP*, 125, 306

Förster, F., González-Gaitán, S., Anderson, J., et al. 2012, *ApJ*, 754, L21

Förster, F., González-Gaitán, S., Folatelli, G., & Morrell, N. 2013, *ApJ*, 772, 19

Gao, F. & Han, L. 2012, *Computational Optimization and Applications*, 51, 259

Giang, N. C., Hoang, T., & Tram, L. N. 2020, *ApJ*, 888, 93

Ginolini, M., Rigault, M., Smith, M., et al. 2025, *A&A*, 695, A140

González-Gaitán, S., de Jaeger, T., Galbany, L., et al. 2021, *MNRAS*, 508, 4656

González-Gaitán, S., Gutiérrez, C. P., Anderson, J. P., et al. 2024, *A&A*, 687, A108

González-Gaitán, S., Gutiérrez, C. P., Martins, G., et al. 2025, *A&A*, 700, A119

Goobar, A. 2008, *ApJ*, 686, L103

Goodman, J. & Weare, J. 2010, *Communications in Applied Mathematics and Computational Science*, 5, 65

Graham, M. L., Valenti, S., Fulton, B. J., et al. 2015, *ApJ*, 801, 136

Gronow, S., Collins, C. E., Sim, S. A., & Röpke, F. K. 2021, *A&A*, 649, A155

Gutiérrez, C. P., González-Gaitán, S., Anderson, J. P., & Galbany, L. 2026, *arXiv e-prints*, arXiv:2602.03599

Gutiérrez, C. P., González-Gaitán, S., Folatelli, G., et al. 2016, *A&A*, 590, A5

Guy, J., Astier, P., Baumont, S., et al. 2007, *A&A*, 466, 11

Guy, J., Sullivan, M., Conley, A., et al. 2010, *A&A*, 523, A7

Hamuy, M., Phillips, M. M., Maza, J., et al. 1995, *AJ*, 109, 1

Hamuy, M., Phillips, M. M., Suntzeff, N. B., et al. 2003, *Nature*, 424, 651

Hamuy, M., Phillips, M. M., Suntzeff, N. B., et al. 1996, *AJ*, 112, 2398

Han, X., Zheng, W., Stahl, B. E., et al. 2020, *ApJ*, 892, 142

Harris, C. R., Millman, K. J., van der Walt, S. J., et al. 2020, *Nature*, 585, 357–362

Hoang, T. 2017, *ApJ*, 836, 13

Hoang, T., Tram, L. N., Lee, H., & Ahn, S.-H. 2019, *Nature Astronomy*, 3, 766

Hoeflich, P., Hsiao, E. Y., Ashall, C., et al. 2017, *ApJ*, 846, 58

Hoeflich, P., Khokhlov, A., Wheeler, J. C., et al. 1996, *ApJ*, 472, L81

Holas, A., Röpke, F. K., Pakmor, R., et al. 2025, *A&A*, 698, A269

Hosseinzadeh, G., Sand, D. J., Valenti, S., et al. 2017, *ApJ*, 845, L11

Hsiao, E. Y., Conley, A., Howell, D. A., et al. 2007, *ApJ*, 663, 1187

Hunter, J. D. 2007, *Computing in Science & Engineering*, 9, 90

Iben, Jr., I. & Tutukov, A. V. 1984, *ApJS*, 54, 335

Inoue, Y., Maeda, K., Nagao, T., & Matsumoto, T. 2025, *arXiv e-prints*, arXiv:2512.10014

Johansson, J., Cenko, S. B., Fox, O. D., et al. 2021, *ApJ*, 923, 237

Jönsson, J., Sullivan, M., Hook, I., et al. 2010, *MNRAS*, 405, 535

Kawabata, K. S., Akitaya, H., Yamanaka, M., et al. 2014, *ApJ*, 795, L4

Kawabata, M., Maeda, K., Yamanaka, M., et al. 2020, *ApJ*, 893, 143

Kelly, B. C. 2007, *ApJ*, 665, 1489

Kelly, P. L., Hicken, M., Burke, D. L., Mandel, K. S., & Kirshner, R. P. 2010, *ApJ*, 715, 743

Kessler, R., Brout, D., D’Andrea, C. B., et al. 2019, *MNRAS*, 485, 1171

Khokhlov, A. M. 1991, *A&A*, 245, 114

Kolmogorov, A. N. 1933, *Giorn Dell’Inst Ital Degli Atti*, 4, 89

Konstantopoulou, C., De Cia, A., Krogager, J.-K., et al. 2022, *A&A*, 666, A12

Kool, E. C., Johansson, J., Sollerman, J., et al. 2023, *Nature*, 617, 477

Kromer, M., Sim, S. A., Fink, M., et al. 2010, *ApJ*, 719, 1067

Lampeitl, H., Smith, M., Nichol, R. C., et al. 2010, *ApJ*, 722, 566

Li, W., Filippenko, A. V., Chornock, R., et al. 2003, *PASP*, 115, 453

Li, W., Wang, X., Bulla, M., et al. 2021, *ApJ*, 906, 99

Little, R. J. A. & Rubin, D. B. 1986, *Statistical Analysis with Missing Data* (New York, NY, USA: John Wiley & Sons, Inc.)

Livne, E. & Glasner, A. S. 1990, *ApJ*, 361, 244

Maeda, K., Bennett, S., Stritzinger, M., et al. 2010, *Nature*, 466, 82

Maeda, K., Leloudas, G., Taubenberger, S., et al. 2011, *MNRAS*, 413, 3075

Maeda, K., Tajitsu, A., Kawabata, K. S., et al. 2016, *ApJ*, 816, 57

Maguire, K., Sim, S. A., Shingles, L., et al. 2018, *MNRAS*, 477, 3567

Maguire, K., Sullivan, M., Patat, F., et al. 2013, *MNRAS*, 436, 222

Mandel, K. S., Narayan, G., & Kirshner, R. P. 2011, *ApJ*, 731, 120

Mannucci, F., Della Valle, M., Panagia, N., et al. 2005, *A&A*, 433, 807

Maoz, D., Mannucci, F., & Nelemans, G. 2014, *ARA&A*, 52, 107

Marino, S., González-Gaitán, S., Förster, F., et al. 2015, *ApJ*, 806, 134

Marion, G. H., Brown, P. J., Vinkó, J., et al. 2016, *ApJ*, 820, 92

Martins, G., González-Gaitán, S., Duarte, J., & Mourão, A. M. 2025, *arXiv e-prints*, arXiv:2511.14332

Matteucci, F. & Recchi, S. 2001, *The Astrophysical Journal*, 558, 351

Maxted, P. F. L. 2025, *Research Notes of the AAS*, 9, 146

McInnes, L., Healy, J., & Astels, S. 2017, *Journal of Open Source Software*, 2, 205

McLachlan, G. J. & Peel, D. 2000, *Finite mixture models* (John Wiley & Sons)

Meldorf, C., Palmese, A., Brout, D., et al. 2023, *MNRAS*, 518, 1985

Mo, G., De, K., Wiston, E., et al. 2025, *ApJ*, 980, L33

Moriya, T. J., Mazzali, P. A., Ashall, C., & Pian, E. 2023, *MNRAS*, 522, 6035

Nagao, T., Maeda, K., & Yamanaka, M. 2018, *MNRAS*, 476, 4806

Ni, Y. Q., Moon, D.-S., Drout, M. R., et al. 2025, *ApJ*, 983, 3

Ni, Y. Q., Moon, D.-S., Drout, M. R., et al. 2023, *ApJ*, 946, 7

Nicolás, N., Rigault, M., Copin, Y., et al. 2021, *A&A*, 649, A74

Nomoto, K. 1980, *Space Sci. Rev.*, 27, 563

Nomoto, K. 1982, *ApJ*, 253, 798

Nomoto, K., Thielemann, F.-K., & Yokoi, K. 1984, *ApJ*, 286, 644

Nugent, A. E., Polin, A. E., & Nugent, P. E. 2023, *arXiv e-prints*, arXiv:2304.10601

Nugent, P. E., Sullivan, M., Cenko, S. B., et al. 2011, *Nature*, 480, 344

O’Donnell, J. E. 1994, *ApJ*, 422, 158

Pan, Y.-C. 2020, *ApJ*, 895, L5

Patat, F., Chandra, P., Chevalier, R., et al. 2007, *Science*, 317, 924

Patat, F., Taubenberger, S., Cox, N. L. J., et al. 2015, *A&A*, 577, A53

Pedregosa, F., Varoquaux, G., Gramfort, A., et al. 2011, *Journal of Machine Learning Research*, 12, 2825

Pérez, E., Cid Fernandes, R., González Delgado, R. M., et al. 2013, *ApJ*, 764, L1

Perlmutter, S., Aldering, G., Goldhaber, G., et al. 1999, *ApJ*, 517, 565

Phillips, M. M. 1993, *ApJ*, 413, L105

Phillips, M. M., Lira, P., Suntzeff, N. B., et al. 1999, *AJ*, 118, 1766

Phillips, M. M., Wells, L. A., Suntzeff, N. B., et al. 1992, *AJ*, 103, 1632

Phillips, M. M. et al. 2013, *ApJ*, 779, 38

Piro, A. L. & Morozova, V. S. 2016, *ApJ*, 826, 96

Piro, A. L. & Nakar, E. 2025, *ApJ*, 993, 63

Polin, A., Nugent, P., & Kasen, D. 2019, *ApJ*, 873, 84

Pollin, J. M., Sim, S. A., Shingles, L. J., et al. 2025, *arXiv e-prints*, arXiv:2507.05000

Popovic, B., Shah, P., Kenworthy, W. D., et al. 2025, *arXiv e-prints*, arXiv:2511.07517

Popovic, B., Wiseman, P., Sullivan, M., et al. 2024, *MNRAS*, 534, 2263

Poznanski, D., Ganeshalingam, M., Silverman, J. M., & Filippenko, A. V. 2011, *MNRAS*, 415, L81

Poznanski, D., Prochaska, J. X., & Bloom, J. S. 2012, *MNRAS*, 426, 1465

Ramaiya, S., Vincenzi, M., Jarvis, M. J., Wiseman, P., & Sullivan, M. 2025, *MNRAS*, 543, 2180

Riess, A. G., Filippenko, A. V., Challis, P., et al. 1998, *AJ*, 116, 1009

Riess, A. G., Yuan, W., Macri, L. M., et al. 2022, *ApJ*, 934, L7

Rigault, M., Brinnel, V., Aldering, G., et al. 2020, *A&A*, 644, A176

Rose, B. M., Garnavich, P. M., & Berg, M. A. 2019, *ApJ*, 874, 32

Ruiter, A. J., Belczynski, K., & Fryer, C. 2009, *ApJ*, 699, 2026

Ruiter, A. J. & Seitenzahl, I. R. 2025, *A&A Rev.*, 33, 1

Scalzo, R. A., Ruiter, A. J., & Sim, S. A. 2014, *MNRAS*, 445, 2535

Sharma, Y., Sollerman, J., Fremling, C., et al. 2023, *ApJ*, 948, 52

Shen, K. J. & Bildsten, L. 2009, *ApJ*, 699, 1365

Shen, K. J., Blondin, S., Kasen, D., et al. 2021, *ApJ*, 909, L18

Shen, K. J. & Moore, K. 2014, *ApJ*, 797, 46

Silverman, J. M., Foley, R. J., Filippenko, A. V., et al. 2012, *MNRAS*, 425, 1789

Simon, J. D., Gal-Yam, A., Gnat, O., et al. 2009, *ApJ*, 702, 1157

Smirnov, N. V. 1939, *Bull. Math. Univ. Moscou*, 2, 3

Soker, N. & Bear, E. 2023, *MNRAS*, 521, 4561

Steinhaus, H. et al. 1956, *Bull. Acad. Polon. Sci.*, 1, 801

Sternberg, A., Gal-Yam, A., Simon, J. D., et al. 2011, *Science*, 333, 856

Sternberg, A., Gal-Yam, A., Simon, J. D., et al. 2014, *MNRAS*, 443, 1849

Stoica, P. & Selén, Y. 2004, *IEEE Signal Processing Magazine*, 21, 36

Stritzinger, M. D., Shappee, B. J., Piro, A. L., et al. 2018, *ApJ*, 864, L35

Sullivan, M., Conley, A., Howell, D. A., et al. 2010, *MNRAS*, 406, 782

Sullivan, M., Le Borgne, D., Pritchett, C. J., et al. 2006, *ApJ*, 648, 868

Taam, R. E. 1980, *ApJ*, 242, 749

The pandas development team. 2020, *pandas-dev/pandas: Pandas*

Thorp, S., Mandel, K. S., Jones, D. O., Ward, S. M., & Narayan, G. 2021, *MNRAS*, 508, 4310

Townsley, D. M., Miles, B. J., Shen, K. J., & Kasen, D. 2019, *ApJ*, 878, L38

Townsley, D. M., Moore, K., & Bildsten, L. 2012, *ApJ*, 755, 4

Toy, M., Wiseman, P., Sullivan, M., et al. 2025, *MNRAS*, 538, 181

Tripp, R. 1998, *A&A*, 331, 815

van Buuren, S. & Groothuis-Oudshoorn, K. 2011, *Journal of Statistical Software*, 45, 1–67

Virtanen, P., Gommers, R., Oliphant, T. E., et al. 2020, *Nature Methods*, 17, 261

Wang, B., Zhou, W.-H., Zuo, Z.-Y., et al. 2017, *MNRAS*, 464, 3965

Wang, X., Chen, J., Wang, L., et al. 2019, *ApJ*, 882, 120

Wang, X., Filippenko, A. V., Ganeshalingam, M., et al. 2009, *ApJ*, 699, L139

Wang, X., Li, W., Filippenko, A. V., et al. 2008, *ApJ*, 677, 1060

Wang, X., Wang, L., Filippenko, A. V., Zhang, T., & Zhao, X. 2013, *Science*, 340, 170

Waxman, E. & Drainey, B. T. 2000, *ApJ*, 537, 796

Wes McKinney. 2010, in *Proceedings of the 9th Python in Science Conference*, ed. Stéfan van der Walt & Jarrod Millman, 56–61

Whelan, J. & Iben, Jr., I. 1973, *ApJ*, 186, 1007

Wiseman, P., Sullivan, M., Smith, M., & Popovic, B. 2023, *MNRAS*, 520, 6214

Wojtak, R. & Hjorth, J. 2025, *A&A*, 702, A176

Woosley, S. E. & Kasen, D. 2011, *ApJ*, 734, 38

Yang, Y., Wang, L., Baade, D., et al. 2018, *ApJ*, 854, 55

Yang, Y., Wang, L., Baade, D., et al. 2017, *ApJ*, 834, 60

Zelaya, P., Clocchiatti, A., Baade, D., et al. 2017, *ApJ*, 836, 88

## Appendix A: Details of fits and measurements

In this section, we show in more detail the photometric, spectroscopic and cosmological measurements performed in sections 2.3, 2.4 and 2.5. A full table with all fitted parameters is presented in App. C.

### Appendix A.1: Photometric fits

The light-curve fitters SiFTO and SNooPy use spectral template series from Hsiao et al. (2007) brought to the observer frame and convolved with the filter transmission to compare the synthetic fluxes with observed multi-band photometry. The time of maximum and the stretch are free parameters. In the case of SiFTO, the stretch parameter  $s$  elongates or compresses the time axis of the  $B$ -band light-curve, spanning values of 0.6 for extremely short-lived 91bg-like objects up to 1.2 for very long-lived, typically 91T-like, SNe Ia. For SNooPy, the colour-stretch  $s_{BV}$  is a measure of the elongation of the colour curve given by the time of its maximum,  $s_{BV} = t_{max,BV}/30d$ , spanning values from 0.3 to 1.3. The other key difference between the two fitters is that SiFTO is agnostic to the reddening law, allowing a free scale parameter for each fitted band, whereas SNooPy assumes stretch-dependent intrinsic colours from which a single scale parameter is fitted and the rest are derived from the dust extinction  $EBV$  and its wavelength dependence  $R_V$ . For best performance, SNooPy should use NIR bands to anchor the reddening law. It uses MCMC for posterior sampling, and we use a uniform prior for  $s_{BV}$ , an exponential decline for  $EBV$  with  $\tau = 0.2$  and a "bin" prior for  $R_V$  that changes according to  $EBV$  (see Burns et al. 2014). To ensure proper estimates of the date of maximum, the light-curve width and the colour or extinction parameters, we require at least four data points between  $-10$  and  $+35$  days from maximum, at least one between  $-10$  and  $+5$ , one between  $+5$  and  $+20$  and at least two filters with data between  $-8$  and  $+10$ . Example fits are shown in Fig. A.1.

In addition to SiFTO and SNooPy, a very popular fitter, especially used in SN Ia cosmology, is SALT (Guy et al. 2007, 2010; Brout et al. 2022b). We do not perform SALT fits in this study, but we compare the overlapping SNe of the PANTHEON+ sample (Brout et al. 2022a) in Fig. A.2. In particular, from a linear fit we find that the stretch division for the two populations of  $\alpha$  values found in Ginolini et al. (2025) of  $x_1 = -0.48$  corresponds to  $s = 0.954$ , very close to the median value of our sample ( $< s > = 0.959$ ).

To fit the late-time Lira law, we require at least three simultaneous  $B$  and  $V$  data points within 35 and 85 days past maximum and a minimum separation of 25 days between the first and last observations. The used photometry is corrected for MW extinction and  $K$ -corrected to the rest-frame. We perform linear fits during this time interval as shown, for example, in Fig. A.3, from which we obtain the Lira slope,  $dBV_{60}$  and intercept  $BV_{60}$ .

### Appendix A.2: Spectroscopic fits

To calculate the expansion velocity of Si II at  $6355\text{\AA}$ , we simply calculate the minimum within a certain region around the line given by the blue- and red-ward edges of Folatelli et al. (2013) (see upper Fig. A.4). To avoid spurious extrema from lower S/N, we first smooth the spectrum with a cosine kernel. The measured uncertainty on the velocity comes from the standard deviation of taking the following 10 minima instead. We also add an uncertainty from the difference in calculating the minimum before and after continuum subtraction. We have compared our methodology

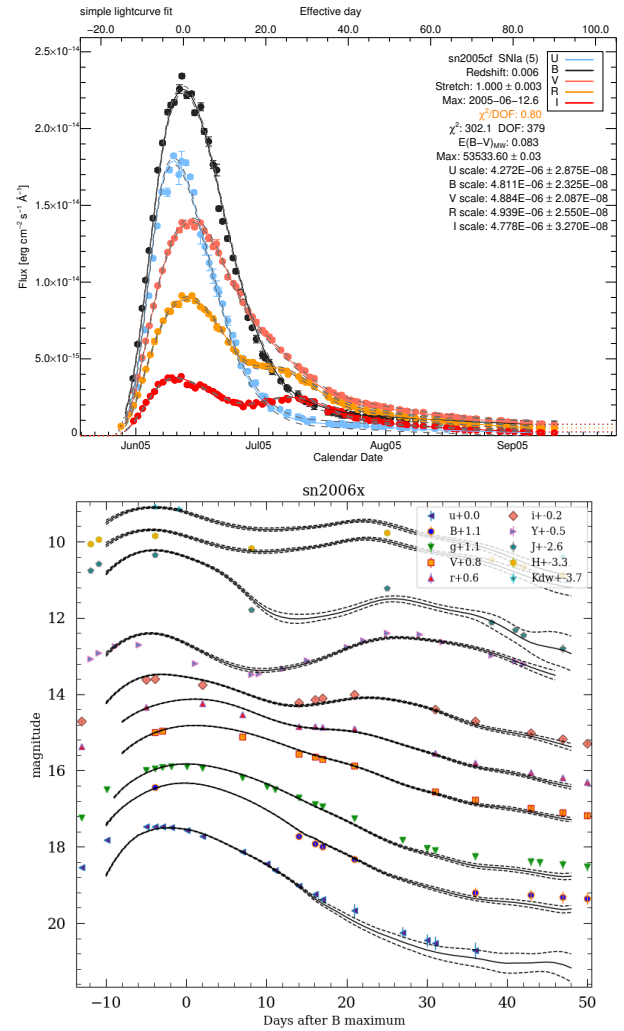


**Fig. A.1.** Example multi-band light-curve fit with SiFTO (upper) for SN 2005cf in  $UVBVR$  flux units and with SNooPy (lower) for SN 2006X in  $uBVgrYHK$  magnitudes.

with the more standard Gaussian-fit approach, finding excellent agreement.

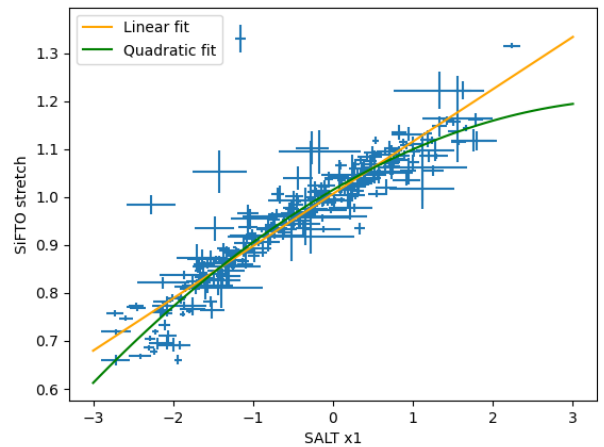


**Fig. A.2.** Comparison of SiFTO stretch  $s$  and SALT  $x_1$  for SNe within our sample and Pantheon+. Linear and quadratic fits are shown.

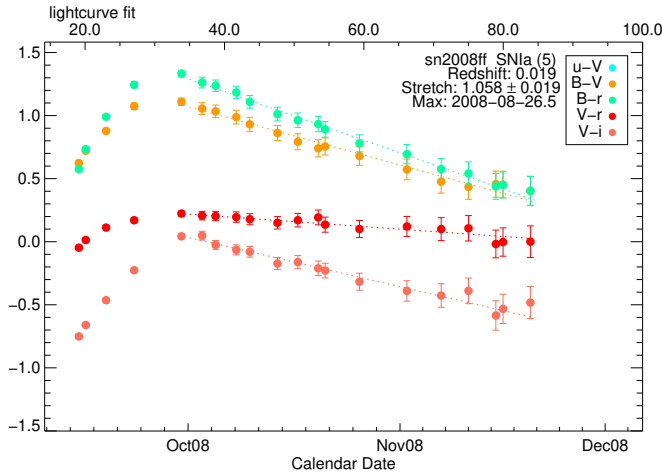


**Fig. A.3.** Example colour-curve for SN 2008ff with Lira-law linear fits (dashed lines) in  $u - B$ ,  $B - V$ ,  $B - r$ ,  $V - r$  and  $V - i$ .

**Table A.1.** Velocity evolution power-law average parameters

Parameter	Median	Higher	Lower
$A$	$4.450 \times 10^3$	$1.146 \times 10^4$	$1.730 \times 10^6$
$t_0$	$-1.618 \times 10^1$	$8.397 \times 10^1$	$-3.468 \times 10^3$
$\gamma$	-0.0666	-0.0155	-0.0523
$C$	$8.893 \times 10^3$	$-8.114 \times 10^3$	$1068 \times 10^4$

**Notes.** Median gradient parameters correspond to  $v_{grad} \sim 60 \text{ km s}^{-1} \text{ d}^{-1}$ , higher gradient to  $v_{grad} \sim 225 \text{ km s}^{-1} \text{ d}^{-1}$  and lower gradient to  $v_{grad} \sim 9 \text{ km s}^{-1} \text{ d}^{-1}$ .

We then use linear or spline interpolation to obtain the velocities at maximum and 20 days after. We require at least one spectrum within  $\pm 3$  days of maximum and one within  $20 \pm 5$  for each of these two measurements, respectively (see lower Fig. A.4). The uncertainty comes from the interpolation of the data uncertainties. When we only have one velocity data point within the range around maximum and no others to interpolate, we use the average power-law fit found for SNe Ia with good coverage (see orange line in the Figure):  $v(t) = A \exp(\gamma(t - t_0)) + C$ , with the fitted values presented in Tab. A.1. We propagate the uncertainties of the parameters for the most extreme high and low velocity gradients shown in the Table.

### Appendix A.3: Cosmological fits

To obtain the best standardisation parameters with a fixed cosmology, we minimise the following log-likelihood for our  $N$  SNe:

$$\ln(\mathcal{L}) = -\frac{1}{2} \sum_{i=0}^N \left[ \frac{\mu_{\text{SN},i} - \mu_{\text{mod},i}}{\sigma_i} + \ln(2\pi\sigma_i^2) \right],$$

with the uncertainty  $\sigma_i$  given only by the diagonal elements of the covariance matrix:

$$\sigma_i^2 = \sigma_{m_B}^2 + (\alpha\sigma_{x_1})^2 + (\beta\sigma_c)^2 - 2\beta\sigma_{m_B,c} + 2\alpha\sigma_{m_B,x_1} - 2\alpha\beta\sigma_{x_1,c} - \sigma_{int}^2 + \sigma_{lens}^2 + \sigma_z^2$$

where  $\sigma_{m_B}$ ,  $\sigma_{x_1}$  and  $\sigma_c$  are the uncertainties associated to SiFTO parameters of each SN, as well as their respective covariances

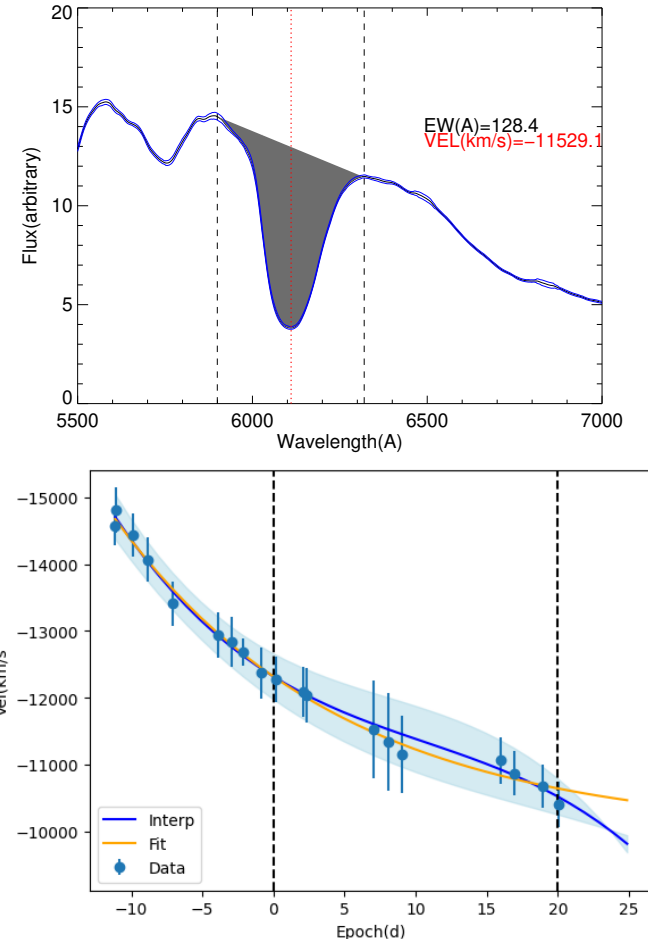


**Fig. A.4.** **Upper:** Example smoothed spectrum of SN 2016coj 7 days after maximum around the Si II 6355 Å line showing the edges of the line (dashed black vertical lines), and the wavelength of the minimum (red dotted line), from which the velocity is calculated. **Lower:** Evolution of the velocity for the same SN, spline interpolation (blue line) and power-law fit (orange). The two characteristic times (0 and 20 days), from which  $v_{grad}$  is calculated, are shown as vertical dashed lines.

$\sigma_{m_B,c}$ ,  $\sigma_{m_B,x_1}$  and  $\sigma_{x_1,c}$ . The parameters  $\sigma_z$  and  $\sigma_{lens}$  correspond to the uncertainty contribution from the redshift uncertainties and from gravitational lensing (Jönsson et al. 2010). Finally,  $\sigma_{int}$  is a free parameter in the fit that accounts for intrinsic variations in the SN luminosities not captured by the standardisation.

We use 10 initial optimisations with the Nelder-Mead algorithm (Gao & Han 2012) implemented in SCIPY, and then do a posterior sampling with a Markov Chain Monte-Carlo (Goodman & Weare 2010) implemented in EMCEE (Foreman-Mackey et al. 2013) with 150 walkers and 800 iterations. An example posterior distribution for the local mass case is shown in Fig. A.5. The final median and  $1\sigma$  uncertainties of the posterior distributions are presented in Tab. 2. The recovered mass-step parameters are 2.2 and  $2.9\sigma$  significant for local and global masses, and the root-mean-square (RMS) of the residuals indicates that a model with global mass-step is slightly preferred. It is important to mention that our very nearby low-redshift sample is biased towards targeted large galaxies (as also seen in the large median stellar mass value of  $\log M_*^G = 10.84$  compared to 10.0 for typical cosmological samples).

A more robust cosmological analysis should include the bias corrections (e.g Kessler et al. 2019) –at least the redshift-dependent Malmquist bias–, as well as non-diagonal covariance

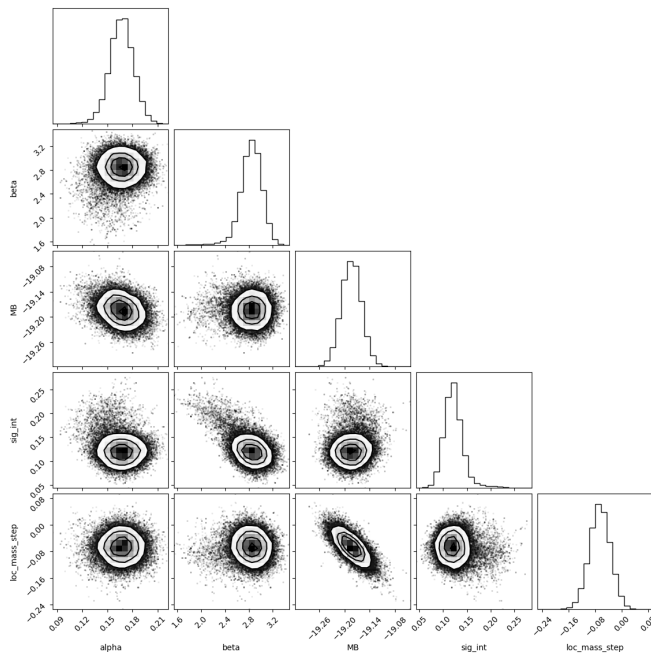


**Fig. A.5.** Corner plot of the posterior distribution of the fitted parameters:  $M_B$ ,  $\alpha$ ,  $\beta$ ,  $\sigma_{\text{int}}$  and  $\Delta_{\text{host}}^L$  for the local stellar mass-step.

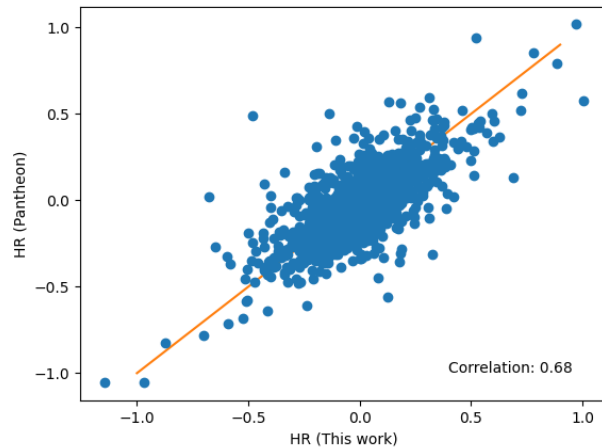


**Fig. A.6.** Comparison of HR obtained in this work with HR from Pantheon+ (Brout et al. 2022a), both without mass-step correction.

elements (e.g., Conley et al. 2011). We stress that the goal of the present study is to evaluate how the HR residuals depend on the narrow line properties of intervening material in the line of sight. As such, the exact values of the fitted parameters, as well as the absolute HR values and their median, are irrelevant; we only care about relative differences between subsamples of SNe Ia. In Fig. A.6, we show that our HR and those of Brout et al. (2022a) without mass-step correction are comparable despite differences in the fitted parameters.

## Appendix B: Details of populations studies

In this section, we expand on the population studies divided according to environment presented in Sect. 3.2, and the clustering analysis presented in Sect. 3.3.

**Table B.1.** Minimum FF test p-value of local environmental properties

Property	$\text{sSFR}^L$	$\text{SFR}^L$	$t_{\text{age}}^L$	$A_V^L$	$M_*^L$
Min p-value	9e-5	2e-4	3e-4	3e-4	8e-4
Division	-11.3	-3.60	1.58	2.51	8.12

**Notes.** The division values are logarithmic for sSFR, SFR and  $M_*$ .

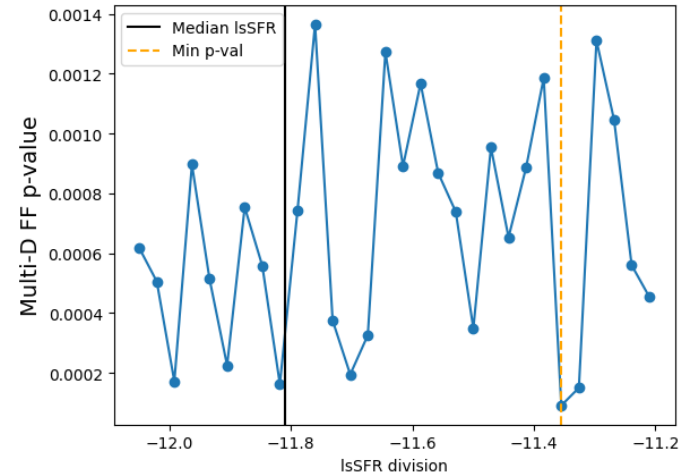


**Fig. B.1.** Multi-dimensional FF test p-value of local environmental properties ( $\text{sSFR}^L$ ,  $t_{\text{age}}^L$ ,  $A_V^L$  and  $M_*^L$ ) as a function of local sSFR division. The median of the sample is shown in black and the sSFR for the minimum p-value in orange.

## Appendix B.1: Environmental subsamples

To obtain two sub-samples of SNe Ia that are significantly different in their environmental properties, we sweep each of the five local properties ( $\text{sSFR}^L$ ,  $\text{SFR}^L$ ,  $t_{\text{age}}^L$ ,  $A_V^L$  and  $M_*^L$ ) within 35 and 65 percentiles of their distributions and calculate for each division the multi-dimensional FF test on the five parameters. An example for the sSFR is shown in Fig. B.1. The minimum p-value is shown with an orange line and occurs at  $\log \text{sSFR} = -11.3$ . Repeating the search with all other environmental parameters as divisions to the sample results in larger p-values (see Tab. B.1). As seen in the Figure, there is no real global minimum, and the exact division between the two samples is somewhat arbitrary.

## Appendix B.2: SFR-corrected distributions

To further demonstrate that the EW of NaID depends on intrinsic SN properties beyond the local environments, we correct here the measured EW for the SFR dependence in a similar way to Paper III. In Fig. B.2 we show the dependence of the EW with SFR that is well fitted by an exponential of the form:  $\text{EW}(\text{SFR}) = a * \log \text{SFR} + b$ , with  $a = 1.13 \pm 0.16$  and  $b = 0.19 \pm 0.03$ . By dividing this dependence of the SFR, we obtain a corrected  $\text{EW}_{\text{corr}} = \text{EW}/\text{EW}(\text{SFR})$ , for which we repeat the analysis presented in Sec. 3.2 and Tab. 5. We confirm the strong differences for all relevant properties such as:  $EBV$ ,  $R_V$ ,  $v_{\text{max}}$  and  $v_{\text{neb}}$ , and reproduce those in Tab. B.2 for the young population. The median EW differences between the two SN distributions are even larger, and their KS p-values are even stronger (except for  $v_{\text{neb}}$ ), confirming that differences in abundance relate to SN properties beyond environments.

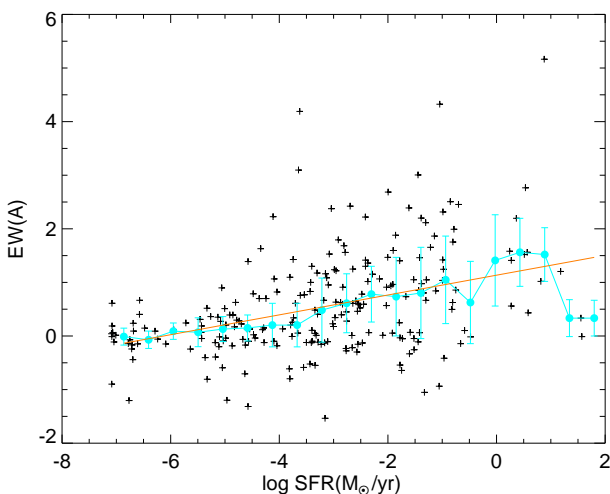


**Fig. B.2.** Na I D EW vs log SFR for SNe (crosses). Median and absolute deviations are shown as cyan circles with error bars, and the orange line represents the best linear fit.

**Table B.2.** KS tests of two  $EW_{corr}$  distributions (corrected by local SFR) divided according to a single property for the young population

Sample		YOUNG		KS	$P_{MC}$
Prop.		$<EW_{hi}>$	$<EW_{lo}>$		
$EBV$		$1.49 \pm 0.60$	$0.47 \pm 0.51$	3.1e-4	81
$R_V$		$0.35 \pm 0.54$	$1.68 \pm 0.69$	7.7e-5	99
$v_{max}$		$0.35 \pm 0.69$	$1.89 \pm 0.48$	2.5e-3	90
$v_{neb}$		$1.49 \pm 1.08$	$-0.37 \pm 0.08$	0.08	6

**Notes.** Similar to Tab. 5 with SFR-corrected EW for a sample of properties.

### Appendix B.3: Clustering subsamples

The Gaussian Mixture Model (GMM, McLachlan & Peel 2000) assumes that the data can be probabilistically represented through a set of normal distributions corresponding to each cluster. We use the scikit-learn implementation (Pedregosa et al. 2011), which starts with a k-means clustering (Steinhaus et al. 1956) to initialise the standardised parameters<sup>4</sup> and then iteratively updates them by fitting the GMM to the data with the Expectation-Maximisation (EM) procedure (Dempster et al. 1977). As input features, we take two local environmental variables,  $SFR^L$  and  $t_{age}^L$ , the stretch  $s$ , the ejecta velocity  $v_{max}$  and the reddening law  $R_V$ .

After finding the clusters and the membership probabilities for each SN, we take into account the uncertainties in the input parameters by doing a Monte Carlo that randomly shifts the input variables according to their covariance matrix. A new set of membership probabilities is calculated in each iteration, and the median probability of the cluster for each SN is calculated. The final membership is given by the highest probability. With this procedure, only 5 out of 106 SNe Ia change their initial membership.

We perform the analysis for two, three and four clusters<sup>5</sup>. For two clusters, the division is strongly related to the local

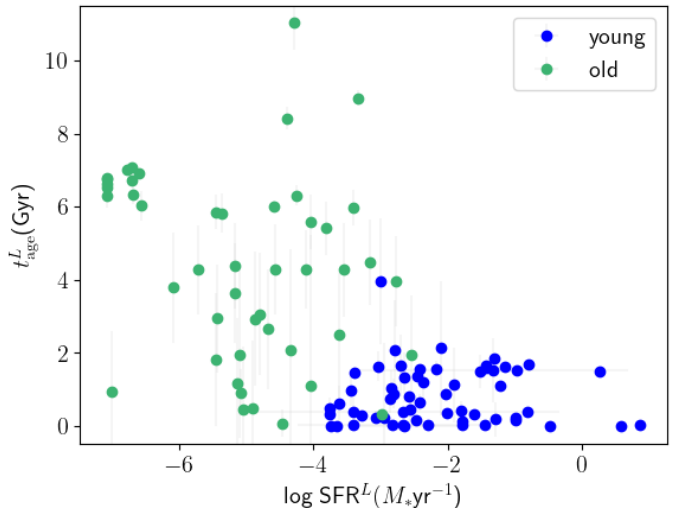


**Fig. B.3.** Local age vs local sSFR for two GMM clusters: "old" and "young".

**Table B.3.** AIC for GMM clusters

GMM	Two	Three	Four
	AIC	1402	1391

environment, as can be seen in Fig. B.3. Three clusters mostly subdivide the young population into two, as shown in Sect. 3.3. A fourth cluster only selects a few outliers. The lowest Akaike Information Criterion (AIC, e.g., Stoica & Selén 2004) is found for three groups as shown in Tab. B.3.

The total sample of SNe Ia used in the clustering consists of 106 objects for which all 5 input features are available. To increase the number of objects in the clustering, we perform a multi-dimensional imputation that replaces missing data with approximate substitute values (Little & Rubin 1986; van Buuren & Groothuis-Oudshoorn 2011). The algorithm is an Iterative Imputation implemented in scikit-learn that does a regression from four features to obtain the fifth feature at each step and for all input features. We only impute SNe for which one of the five features is lacking. More importantly, the imputation is used only to find membership labels for an increased population of 192 SNe, but all the properties shown in Fig. 6, as well as the statistics presented in Tab. B.4 and Fig. B.4 were obtained with real non-imputed values.

In general, we recover the results of the initial sample with the increased imputed population. Interestingly, the fraction of "young-receding" SNe Ia becomes larger (from 47% to 60% of the young population), perhaps indicating that these are more frequent. However, the local age difference between young-receding and young-approaching SNe Ia becomes larger and is accompanied also by a decrease in the p-values of the light-curve parameters ( $s$  and  $s_{BV}$ ). This could indicate some leakage of older, short-lived SNe Ia into the young-receding population. Some of the characteristics for the young-approaching sample are further strengthened: the  $v_{max}$ ,  $v_{grad}$ ,  $R_V$ , and all colour properties ( $C$ ,  $EBV$  and  $BV_{60}$ ) have even lower p-values that further differentiate from the other clusters.

<sup>4</sup> Parameters are subtracted by the mean and divided by the standard deviation to give each input feature the same weight.

<sup>5</sup> We also employed another clustering techniques for which the number of clusters is not enforced (HDBSCAN, McInnes et al. 2017), but the number of noise elements encountered by the algorithm was too large.

**Table B.4.** Median properties for three SN clusters: "old", "young-receding", and "young-approaching" for the imputed sample.

Property	Cluster		
	OLD	YOUNG-RECEDING	YOUNG-APPROACHING
Nr	69	74	49
EW	$-0.01 \pm 0.25$	$0.27 \pm 0.38$	$1.36 \pm 0.75$
VEL	$-22 \pm 177$	$127 \pm 286$	$-67 \pm 282$
$\Delta\alpha$	$0.37 \pm 0.11$	$0.16 \pm 0.07$	$0.11 \pm 0.04$
<b>SFR<sup>L</sup></b>	$-5.03 \pm 1.06$	$-2.65 \pm 1.14$	$-2.29 \pm 0.90$
<b><math>t_{age}^L</math></b>	$5.72 \pm 1.98$	$0.64 \pm 0.63$	$0.74 \pm 0.71$
<i>s</i>	$0.91 \pm 0.09$	$0.93 \pm 0.12$	$0.98 \pm 0.05$
<i>C</i>	$0.05 \pm 0.07$	$0.09 \pm 0.10$	$0.24 \pm 0.18$
$s_{BV}$	$0.90 \pm 0.09$	$0.88 \pm 0.16$	$0.96 \pm 0.07$
$EBV$	$0.20 \pm 0.10$	$0.21 \pm 0.10$	$0.37 \pm 0.18$
<b><math>R_V</math></b>	$3.89 \pm 1.55$	$4.29 \pm 1.03$	$2.08 \pm 0.62$
$dBV_{60}$	$-0.012 \pm 0.002$	$-0.011 \pm 0.003$	$-0.012 \pm 0.003$
$BV_{60}$	$0.84 \pm 0.12$	$0.83 \pm 0.14$	$1.06 \pm 0.15$
$v_{max}$	$-10761 \pm 573$	$-10642 \pm 388$	$-12351 \pm 1064$
$v_{grad}$	$69.6 \pm 29.2$	$69.3 \pm 21.7$	$96.0 \pm 48.6$
$v_{neb}$	$-119 \pm 639$	$621 \pm 776$	$1905 \pm 784$
HR	$0.05 \pm 0.14$	$0.00 \pm 0.08$	$-0.03 \pm 0.12$
$HR_L$	$0.04 \pm 0.13$	$0.01 \pm 0.08$	$-0.06 \pm 0.14$
$HR_G$	$0.06 \pm 0.11$	$0.02 \pm 0.06$	$-0.07 \pm 0.12$

**Notes.** Property, median and MAD for three clusters: old, young-receding and young-approaching for imputed of 192 SNe. The five input properties for the clustering are highlighted in bold.

## Appendix C: List of properties

We provide in electronic format the full set of properties for all objects used in this study. The table C.1 shows the columns of that table.

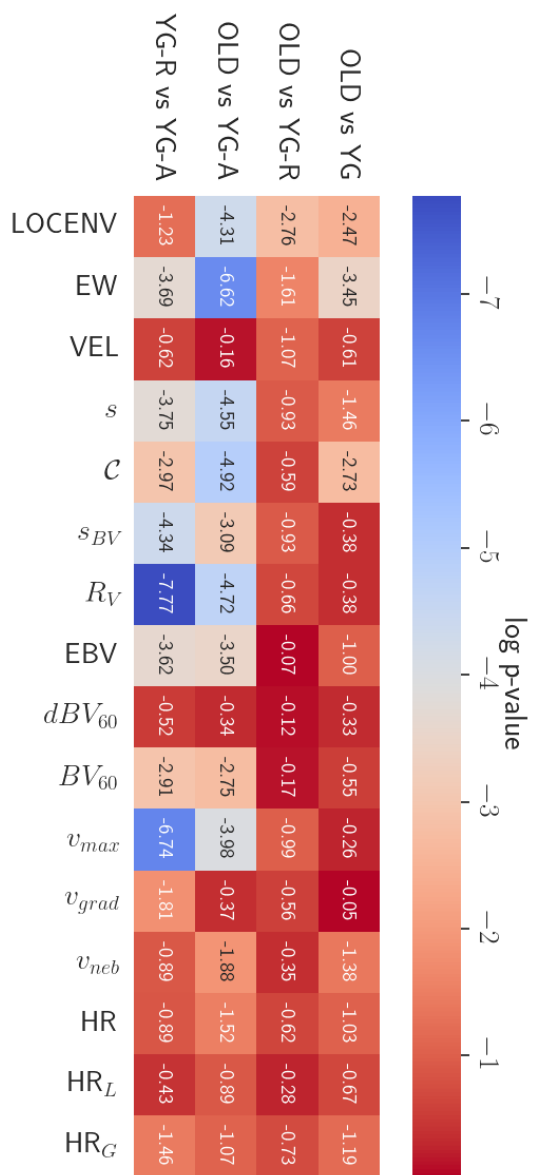


**Fig. B.4.** Similar to Fig. 8 for the total imputed sample.

**Table C.1.** Column description of electronic table of SN Ia and host properties.

Column	Property	Column	Property
1	SN name	23	$\sigma(C)$
2	Redshift	24	$s_{BV}$
3	EW	25	$\sigma(s_{BV})$
4	$\sigma(\text{EW})$	26	$EBV$
5	VEL	27	$\sigma_{EBV}$
6	$\sigma(\text{VEL})$	28	$R_V$
7	$\Delta\alpha$	29	$\sigma(R_V)$
8	$\log \text{sSFR}^L$	30	$dBV_{60}$
9	$\sigma(\log \text{sSFR}^L)$	31	$\sigma(dBV_{60})$
10	$\log \text{SFR}^L$	32	$BV_{60}$
11	$\sigma(\log \text{SFR}^L)$	33	$\sigma(BV_{60})$
12	$t_{\text{age}}^L$	34	$v_{\text{max}}$
13	$\sigma(t_{\text{age}}^L)$	35	$\sigma(v_{\text{max}})$
14	$A_V^L$	36	$v_{\text{grad}}$
15	$\sigma(A_V^L)$	37	$\sigma(v_{\text{grad}})$
16	$M_*^L$	38	$v_{\text{neb}}$
17	$\sigma(M_*^L)$	39	$\sigma(v_{\text{neb}})$
18	$M_*^G$	40	HR
19	$\sigma(M_*^G)$	41	$\text{HR}_L$
20	$s$	42	$\text{HR}_G$
21	$\sigma(s)$	43	Cluster member <sup>†</sup>
22	$C$	44	LC source <sup>*</sup>

**Notes.** The units of all properties are shown in Tab. 1.

<sup>†</sup> Cluster membership of each SN when available (see Sect. 3.3).

<sup>\*</sup> References of the SN photometry used for light-curve fits.